

國立交通大學  
光電工程研究所

碩士論文

氮化鎵二維面射型光子晶體雷射閾值增益之研究

*The Study of Threshold gain in GaN-Based 2D  
Photonic Crystal Surface Emitting Lasers*

The logo of Tsinghua University is a circular seal. It features a gear-like outer border. Inside the circle, there is a shield-shaped emblem. The emblem contains the letters 'ES' at the top, 'A' on the right, and '1896' at the bottom. The entire logo is rendered in a light purple color.

研究生：翁鵬翔

指導教授：郭 浩 中 教授

盧 廷 昌 教授

中華民國九十九年七月

氮化鎵二維面射型光子晶體雷射閾值增益之研究

The Study of Threshold gain in GaN-Based  
2D Photonic Crystal Surface Emitting Lasers

研 究 生：翁鵬翔

Student：Peng-Hsiang Weng

指導教授：郭浩中

Advisors：Hao-Chung Kuo

盧廷昌

Tien-Chang Lu



A thesis

Submitted to Institute of Electro-Optical Engineering  
College of Electrical Engineering and Computer Science

National Chiao Tung University

In partial Fulfillment of the Requirements

for the Degree of Master

in

Electro-Optical Engineering

July 2010

Hsinchu, Taiwan, Republic of China

中 華 民 國 九 十 九 年 七 月

# 氮化鎵二維面射型光子晶體雷射閾值增益之研究

研究生：翁鵬翔

指導教授：郭浩中 教授

盧廷昌 教授

國立交通大學 光電工程研究所

## 摘 要

本篇論文旨在利用多重散射法模擬不同結構設計下造成二維面射型光子晶體雷射之閾值增益變化。根據光子晶體的布拉格理論，光子晶體必須滿足特定的布拉格繞射條件才能產生雷射。我們研究部份，則著重於在面射型出光的  $\Gamma_2$  能帶。我們將分為三個部分討論在不同結構變化下對於面射型光子晶體雷射的影響。第一部分討論當光子晶體層數改變時對閾值增益及正規劃頻率的變化。我們發現當層數超過 20 層時，光子晶體的影響將會趨緩且正規化頻率會趨近能帶邊緣。第二部分，藉由改變空氣填充因數來研究不同的模態，面射型光子晶體雷射的雷射閾值增益。第三部分，我們設計了不同 PCSELs 邊界條件。發現圓形邊界比一般六角邊界有著更低的閾值增益。最後，根據模擬結果，我們在 GaN 材料發光二極體上設計了，在  $\Gamma_2$  點附近，晶格常數約 190nm 的面射型光子晶體雷射。

# ***The Study of Threshold gain in GaN-based 2D Photonic Crystal Surface Emitting Lasers***

**Student : Peng-Hsiang Weng**

**Advisor: Huo-Chung Kuo  
Tien-Chang Lu**

Institute of electro-optical Engineering  
National Chiao-Tung University

## **Abstract**

In this thesis, we investigated the different lasing behaviors of threshold gain in GaN-based 2D photonic crystal surface emitting lasers (PCSELs) according to Multiple Scattering Method (MSM). Based on the Bragg diffraction theory for PCs period structure, the lasing behavior could only be happened when the Bragg condition is satisfied. Our studies are especially focused on the band edge at  $\Gamma_2$  point because of the characteristic of photonic crystal surface emitting. In our study, we divide research into three parts to study the different effect of structure on PCSELs. At first, we change the number of shell for PCSELs that would affect the threshold gain and normalized frequency. When the number of shell is over 20, the influence of photonic crystal will decrease. Secondly, we modify the filling factor of photonic crystal to optimize the threshold gain parameter for PCSELs. The four  $\Gamma_2$  point band-edge of PCSELs have different lasing threshold gain distribution. Finally, we consider the boundary condition for our PCSELs. The circle boundary has the lower threshold gain than the usual hexagonal boundary. As a result, we designed the PCs lattice constant about 190nm for  $\Gamma_2$  point lasing, and successfully fabricated the PCs structure on our novel GaN-based resonance cavity light emitting diode.

## 致謝

在交大碩士班兩年的日子，即將要結束了，在這兩年當中發生了許多難忘的事情，參加了許多自己以前沒有嘗試過的比賽，這個碩士班兩年過很值得、很有趣，會是我一輩子難以忘懷的回憶。

首先，就先來聊聊實驗室的部分吧！在王興宗老師身上，我看到了一代大師的風範，嚴謹的研究方式，及開朗的生活態度，是大家學習的楷模；而郭老師在業界的人脈及管理團隊的能力，讓我相當欣賞及佩服，希望未來有機會能跟老師合作；盧老師總是不厭其煩的跟我討論研究上面的問題，最後我們才有機會做出不錯的研究成果。也感謝學長姐們的大力相挺，清華、博孝、士偉、宗鼎、小馬、阿綱…，沒有你們我的實驗是無法順利完成的，另外在你們身上學習到不同的研究態度及生活方式，也會是我做為未來參考的重要經驗。

碩士班同學阿祥、小昕、宅 Jo、阿菲、依寧、祥琪、阿吉、獸皇、小邱、彥群、惟雯、David、哭哭、小胖，跟大家玩在一起的日子很有趣，如今要各奔東西了，總是有一絲絲的”捨不得”，希望之後大家能夠再聚在一起。學弟昀霖、幼齒、阿國、Jolin…，有你們的幫忙及協助，讓我體會到許多實驗的樂趣！特別感謝中央大學樂丕綱教授及江陣余學長，你們不藏私的教導及分享，才讓我能完成這份碩士班論文。

課外活動部分，謝謝 YEF 讓我有機會去嘗試到除了理工之外的領域，也給了我機會讓我出國參訪，看到了更大更廣的世界，YEF 的夥伴們也會是一起創業的重要資產喔！

感謝我的家人，你們總是無條件在我背後支持我，不論順利或失敗，你們的安慰，是讓我有繼續努力的原動力！

最後，感謝我的女朋友瑤嫻，有你的陪伴，才讓我的碩班生涯不孤單，有著更多精彩多姿的回憶！

# Contents

<b>Abstract (in Chinese).....</b>	<b>I</b>
<b>Abstract (in English).....</b>	<b>II</b>
<b>Acknowledgement.....</b>	<b>III</b>
<b>Contents.....</b>	<b>IV</b>
<b>Figure Contents.....</b>	<b>VI</b>

## **Chapter 1 Introduction**

1.1 Nitride-based materials.....	1
1.2 Photonic crystal lasers in nitride-based materials.....	2
1.2.1 2D PC Nano-Cavity Lasers .....	3
1.2.2 2D PC Band-edge lasers .....	4
1.3 Objective of the thesis .....	5
1.4 Outline of the thesis .....	6
References .....	7

## **Chapter 2 Fundamentals of Photonic Crystal Surface Emitting Lasers**

Introduction .....	8
2.1 Bragg diffraction in 2D Photonic Crystal .....	9
2.2 Multiple Scattering Method .....	14
2.2.1 2D Gain rod .....	14
2.2.2 Multiple scattering of light by gain rod array.....	15
2.3 Multiple Scattering Method for PCSELS .....	21
2.3.1 Threshold gain Simulation.....	22
2.3.2 Resonant Mode Simulation.....	23
2.3.3 Reciprocal space (K-Space) Simulation .....	25

References .....	28
<b>Chapter 3    Fabrication of GaN-based 2D Photonic Crystal Surface Emitting Lasers</b>	
3.1    Wafer Preparation .....	29
3.2    Process Procedure .....	31
3.3    Process flowchart .....	34
<b>Chapter 4    Simulation and Experiment Results of GaN-based 2D Photonic Crystal Surface Emitting Lasers</b>	
4.1    The design for PCSELs .....	37
4.2    The effect of the number of shells for PCSELs.....	41
4.3    The effect of Photonic Crystal Filling Factor.....	43
4.4    The effect of Photonic Crystal Boundary.....	45
References .....	49
<b>Chapter 5    Conclusion .....</b>	<b>50</b>
<b>Appendix</b>	

## Figure Contents

- Fig 2-1 (a) The band diagram and different band edges of triangular lattice photonic crystal. (b) The schematic diagram of reciprocal space.
- Fig 2-2 Wave vector diagram at point (A)M1 (B)K1 (C)  $\Gamma$ 2 (D) M2 (E) K2 (F) M3,  $k_i$  and  $k_d$  indicate incident and diffracted light wave
- Fig 2-3 The wave vector diagram at point  $\Gamma$ 2,K2,M3 in vertical direction
- Fig 2-4 Geometry of multiple scattering method of circular cylinders and coordinate system.
- Fig 2-5 The peak is indicated the normalized frequency and threshold amplitude gain  $K_{am}''$  at the calculated lasing modes.
- Fig 2-6. Poynting vector (light-energy flow) and electric field distribute in real space for different close-to-lasing PC modes. The amplitudes of the fields are shown by the contours the intensity increases in the order blue to red. The rod array is displayed as circles.(a) the simulation results of reference (b) our simulation results to match the paper figures.(c) electric field distributions.
- Fig 2-7 The field distributions of different band-edge modes on band diagram.
- Fig 2-8 The K-space distributions of different band-edge modes for PCSEL. These are used Fast Fourier Transform method by Eq (2.31)
- Fig 3-1 The schematic diagram of nitride structure grown by MOCVD.
- Fig 3-2 SEM images of plane view and cross section of PC pattern.
- Fig 3-3 Process flow chart of PCSELs, steps are ordered from (a) to (f).
- Fig 3-4 Complete PCSELs' device after removing SiNx film.
- Fig 4-1 The lowest guided mode optical field distribution, where the confinement factor  $\Gamma_g = 0.8625$  and  $n_{eff} = 2.482$ .
- Fig 4-2 Left: Complete band structure; Right: The magnified band structure around  $\Gamma$ 2 modes.
- Fig 4-3 (a)-(f) are the magnetic field distributions of six modes in Figure 4-2 .Blue and red areas correspond to positive and negative magnetic fields



perpendicular to the plane. Black circles indicate lattice points.

Fig 4-4 Normalize frequency would shift near band edges for different PC Shell (N values). The horizontal dash line indicates the normalized frequency of band edge calculated from PWEM.

Fig 4-5 Threshold gain as a function of the number of air-hole layers (N) for  $\Gamma_2$  band-edge resonance of a 2D photonic crystal.

Fig 4-6 Normalized resonant mode frequencies as a function of the filling factor, calculated using (a) the Multiple Scattering Method, and (b) the 2D PWEM

Fig 4-7 The threshold gains for the four modes as functions of the hole-filling factor.

Fig.4-8 (a) Schematic drawing of the device with different boundaries. (b) SEM pictures of two kind of PCSELS (c) The electric field distributions

Fig.4-9 Measured output intensity versus input excitation energy density from the GaN-based PCSELS with bottom AlN/GaN distributed Bragg reflectors at room temperature.(a)The threshold energy density of hexagonal boundary is about  $3.2\text{mJ/cm}^2$ .(b) The threshold energy density of circle boundary is about  $2.85\text{ mJ/cm}^2$ .

# Chapter 1

## Introduction

### 1.1 Nitride-based materials

Over the past decade, Nitride-based materials has been attracting much attention because of their large direct wide band-gap characteristics and can be widely used in various optoelectronic devices such as flat panel displays, optical storage, automobiles, illumination and so on[1-4]. According to the large band off-set characteristic of these kinds of III-V wide band-gap materials, which can be utilized in hetero-structure and can provide better carrier confinement to increase the efficiency of the whole structure. Their wide-range band-gap also provides possibility of full-color emission because they cover red, green, and blue emission regions. The property further makes nitride based materials more and more important for the applications of full-color display or solid-state lighting by light emitting diodes (LED) and laser diodes (LD). Moreover, nitride-based materials still have lots of advantages such as operation in higher temperature and the higher peak drift velocity for electron. Especially in GaN, the material shows greater characteristic with high bond energy ( $\sim 2.3\text{eV}$ ), high saturation velocity ( $\sim 2.7 \times 10^4 \text{ cm/s}$ ), high breakdown field ( $\sim 2 \times 10^6 \text{ V/cm}$ ) and strong excitonic energy ( $> 50\text{meV}$ ). Because of these advantages, the GaN-based device plays an important role of the high efficiency electro-optic applications and products. However, the problems in GaN, AlN, and its alloy materials are including large defect densities, piezoelectric field effect and spontaneous polarization. It reveals the most important thing is growing defect-frees material to fabricate high quality and high power devices. Nowadays, the GaN-based materials with its superior properties make it a good candidate for the optoelectronic applications in next generation.

## 1.2 Photonic crystal in nitride-based materials

During the last decade, there has been considerable interest in photonic band gap materials or photonic crystals due to their ability to control the properties of light emission and propagation. Many studies have contributed to realize the PC cavities in GaAs-based material by e-beam lithography technique. Since GaN and related nitrides have been the most promising laser diode material in the blue-violet-ultraviolet region, the optical properties of photonic crystal in GaN material is what people want to investigate, recently. As we know, photonic crystal is a dielectric structure arranged in periodic geometry. Like a crystalline solid in electronic band structure. So photonic crystal can exhibit one or more photonic band gaps (PBGs), with frequency in band gap unable to propagate in the crystal. Photonic crystal with photonic band gaps for photons have many advantages in controlling the light emission, wave propagate along specific direction and can be utilized in many optoelectronic devices [5]. For instance, photonic crystal passive waveguide used as low loss channel for light propagation and resonator to keep the whole cavity with high Q characteristic, which can be a promising device in conjunction with Si based and III-V materials communication system. Semiconductor with these unique properties can not only be used as a versatile building block to construct photonic circuitry but also an active medium to control light emission [6]. Two kinds of semiconductor photonic lasers have been demonstrated. One is 2D photonic crystal nano-cavity lasers, and the other is 2D photonic crystal band-edge lasers.

### 1.2.1 2D PC Nano-Cavity Lasers

In 1994, P. R. Berman et al. first presented the mechanism that photonic crystal could be a reflective mirror to form a cavity and achieve the laser operation [7]. Then, in 1999, O. Painter practically demonstrated an optically pumped InGaAs-based 2-D PC nano-cavity laser emitting at 1.55 micrometers [8]. The optical cavity he demonstrated was consisted of a half-wavelength-thick waveguide for vertical confinement and a 2-D PC mirror for lateral localization. A defect was introduced as a nano-cavity because the mode volume was 2.5 cubic half-wavelength widths, approximately 0.03 micrometers, in the 2-D PC to trap photons inside. In 2004, H. G. Park et al. realized the electrically driven single-cell 2-D PC laser with a dominated wavelength at 1519.7 nm [9]. They used a sub-micrometer-sized semiconductor post located at the center of the single-cell photonic crystal resonator to connect bottom electrode and achieved lasing action by current injection. The result is the first current injection report in the world. However, the nitride-based photonic crystal nano-cavity laser never be observed in recently few decades. Fortunately, in 2005, nitride-based photonic crystal nano-cavity membrane emitted at 488nm with quality factor Q of about 800 was reported by Y. S. Choi et al. [10]. They used photo-enhanced chemical etching to form a GaN-based membrane with a total thickness of nearly 140 nm and patterned a photonic crystal nano-cavity on it. Some resonance modes from the nano-cavity with photonic crystal lattice constant of about 180 nm could be observed in the photoluminescence (PL) emission.

### 1.2.1 2D PC Band-edge lasers

The second one is the photonic crystal band edge laser. According to the DFB theory, light at the photonic band-edge has zero group velocity and forms a standing wave due to 2D DFB effect. Specific band-edges induce not only in-plane coupling via DFB, but also diffraction normal to the PC plane, causing surface emission phenomena. In 1999, Noda et al. reported the electrically driven 2-D PC band-edge laser under pulsed operation [11]. The PC was a triangular-lattice structure composed of InP and air holes, which is integrated with an InGaAsP/InP multiple-quantum-well active layer by a wafer fusion technique. They demonstrated the single-mode, large-area and surface-emitting lasing action, and analyzed the lasing mechanism based on the satisfying of Bragg condition. Then, they further reported the room-temperature (RT) 2D PC band-edge laser under continuous wave (CW) operation in 2004 [12]. In 2008, Noda's group had demonstrated the GaN PCSELS room temperature operation by current injection; they also measured the angle-resolved diagram around  $\Gamma$  band-edge mode [13].

### 1.3 Objective of the thesis

During the past few decades, a considerable amount of literature about photonic crystal surface emitting lasers utilizing a 2-D distributed feedback (DFB) mechanism has been published and reported. There also have many different simulation methods to figure out photonic crystal laser. For example, we can get band diagram by the Plane Wave Expansion Method (PWEM) to understand the relationship between energy and wave number. Moreover, many simulation results are based on FDTD because FDTD method could simulate the real structure more precise. However, FDTD method consumes numerous computer memories and time. Thus, we choose the more simple and convenient Multiple Scattering Method (MSM) to investigate the oscillation mechanism for PCSELS. Multiple scattering method could simulate the information such as threshold gain, electric field, wave vector and pointing vector distributions for PCSELS. It is useful to optimize designs for PCSELS and to realize lasing phenomenon of photonic crystal.

This thesis presents a theoretical method to calculate the lasing phenomena that occur in PCSELS having optical gain in their background material. We especially focus on the behavior of threshold gain of PCSELS in the research. We demonstrate the number of photonic crystal influence about threshold gain and normalized frequency. Then, we discuss the filling factor effect for PCSELS by MSM and compare results with PWEM. Finally, we compare simulation results for hexagonal and circle boundary PCSELS to clarify the feedback mechanisms in real PCSELS. The theoretical approach taken in this paper for the analysis of lasing phenomena could also be applied to other kinds of lasers such as whispering-gallery-mode lasers, random lasers, and photonic quasi-crystal lasers.

## 1.4 Outline of the thesis

This thesis has been organized in the following arrangement. The first chapter of the paper will introduce the history of nitride-based materials and different types of photonic crystal laser. Chapter 2 begins by laying out the theoretical dimensions of the research, the Multiple Scattering Method and oscillation feedback mechanism. Chapter 3 describes the wafer preparation, fabrication and design of PCSELs. Chapter 4 describes the simulation results, characteristics and experiment result of PCSELs. The last chapter assesses the conclusion and future work.



## References

- [1] S. Nakamura, M. Senoh, N. Iwasa, and S. Nagahama, Jpn. J. Appl.Phys., 34, L797 (1995)
- [2] S. Nakamura, T. Mukai, and M. Senoh, Appl. Phys. Lett.,64, 1687 (1994)
- [3] S. Nakamura, M. Senoh, S.Nagahama, N.Iwasa, T. Yamada, T. Matsushita, Y. Sugimoto, and H.Kiyoku, Appl. Phys. Lett., 70, 868 (1997)
- [4] S. Nakamura, Science, 281, 956 (1998)
- [5] M. Notomi, Phys. Rev. B 62, 10696–10705 (2000)
- [6] C.M. Lai, H. M. Wu, P. C. Huang, S. L. Peng, Appl. Phys. Lett., 90, 141106, (2007)
- [7] P. R. Berman, New York:Academic, (1994)
- [8] O. Painter, R. K. Lee, A. Scherer, A. Yariv, J. D. O'Brien, P. D. Dapkus, I. Kim, Science,284, 1819, (1999)
- [9] H. G. Park, S. H. Kim, S. H. Kwon, Y. G. Ju, J. K. Yang, J. H. Baek, S. B. Kim, Y. H. Lee, Science, 305, 1444, (2005)
- [10] Y. S. Choi, K. Hennessy, R. Sharma, E. Haberer, Y. Gao, S. P. DenBaars, C. Meier, Appl. Phys. Lett., 87, 243101, (2005)
- [11] M. Imada, S. Node, A. Chutinan. and T. Tokuda, Appl. Phys. Lett., 75, 316, (1999)
- [12] D. Ohnishi, T. Okano, M. Imada, and S. Node, Opt. Exp., 12, 1562, (2004)
- [13] Hideki Matsubara, Susumu Yoshimoto, Hirohisa Saito, Yue Jianglin, Yoshinori Tanaka, Susumu Noda, Science, 319, 25 JANUARY, (2008)



## **Chapter 2**

# **Fundamentals of Photonic Crystal Surface Emitting Lasers**

### **Introduction**

A considerable amount of literature has been published on photonic crystal surface emitting laser utilizing a 2D distributed feedback (DFB) mechanism [1-4]. The device features single longitudinal and transverse mode, lasing with large area and narrow beam divergence. Thus, there have been many theoretical analysis and methods developed, such as 2D plane wave expansion method [5](PWEM), finite difference time domain [6-7](FDTD), Transfer Matrix, Couple Mode Theory and Multiple Scattering Method, etc to simulate properties of photonic crystal laser. There are different advantages and limitations while using these theoretical methods. For example, 2D PWEM only applies to the infinite that is contradictory to actual device. FDTD method consumes numerous computer memories to simulate the real structure. Thus, we decide to combine the Transfer Matrix and Multiple Scattering Method to calculate real structure of photonic crystal surface emitting laser. Moreover, we applied the imaginary part of refractive index to investigate threshold gain enhancement and threshold frequency. Thus, we could get the more accurate simulation results for our experiment results. In this chapter, first part is the fundamental of Bragg diffraction in 2D photonic crystal, then focus on the fundamental of Multiple Scattering Method in gain material.

## 2.1 Bragg diffraction in 2D Photonic Crystal [8],[9]

Fig 2.1(a) shows a band diagram of a triangular-lattice photonic crystal. The points (A), (B), (C), (D), (E) and (F) are the points  $M_1$ ,  $K_1$ ,  $\Gamma_2$ ,  $M_2$ ,  $K_2$  and  $M_3$ , respectively. The reciprocal space of the structure is a space combined by hexagons. Fig 2.1(b) shows a schematic diagram of a reciprocal space. The  $K_1$  and  $K_2$  are the Bragg vectors with the same magnitude,  $|K|=2\pi/a$ , where  $a$  is the lattice constant of the photonic crystal. Consider the transverse modes in the 2-D photonic crystal structure, the diffracted light wave from the structure must satisfy the relationship:

$$k_d = k_i + q_1 K_1 + q_2 K_2, \quad q_{1,2} = 0, \pm 1, \pm 2, \dots \quad (2.1)$$

$$\omega_d = \omega_i \quad (2.2)$$

where  $k_d$  is xy-component wave vector of diffracted light wave,  $k_i$  is xy-component wave vector of incident light wave,  $q_{1,2}$  is order of coupling,  $\omega_d$  is the frequency of diffracted light wave, and  $\omega_i$  is the frequency of incident light wave. Eq. (2.1) represents the phase-matching condition (or momentum conservation), and Eq. (2.2) represents the constant-frequency condition (or energy conservation). When both of equations are satisfied, the lasing behavior would be observed.

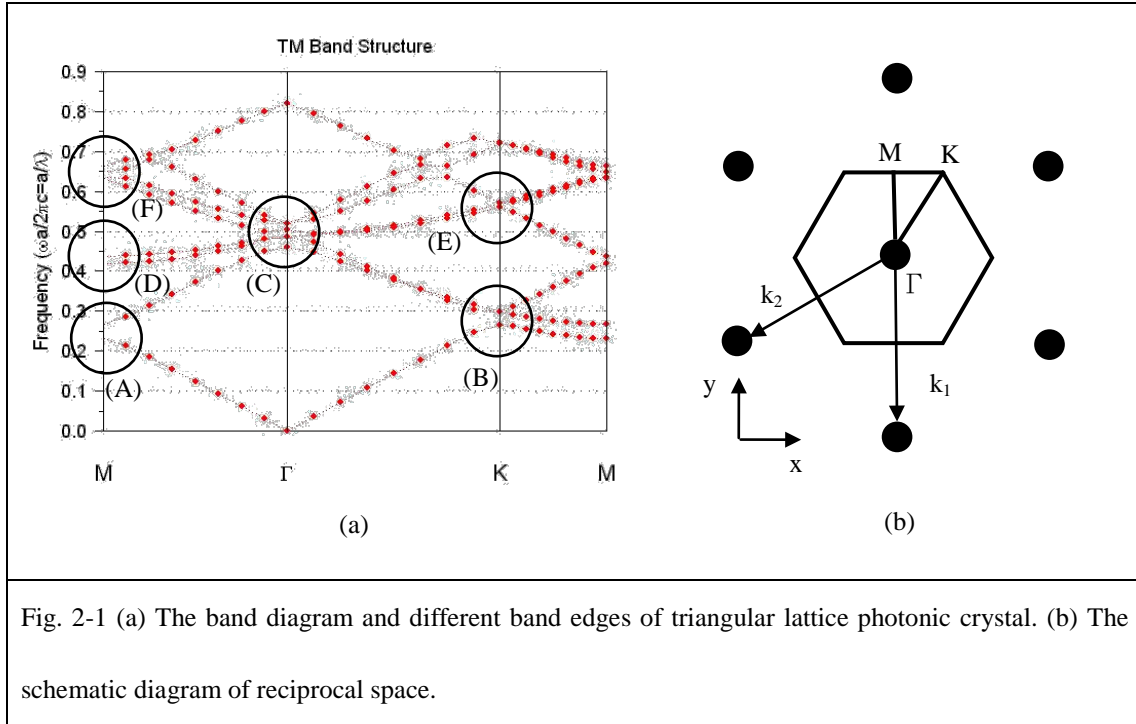


Fig. 2-1 (a) The band diagram and different band edges of triangular lattice photonic crystal. (b) The schematic diagram of reciprocal space.

It is expected lasing occurs at specific points on the Brillouin-zone boundary ( $\Gamma$ , M, and K) and at the points at which bands cross and split. At these lasing points, waves propagating in different directions couple to significantly increase the mode density. It is particularly interesting that each of these points exhibits a different type of wave coupling. For example, as shown in Fig 2.3(a), the coupling at point M1 only involves two waves, propagating in the forward and backward directions. This coupling is similar to that of a conventional DFB laser. However, there can be six equivalent  $\Gamma$ -M directions in the structure; that is, the cavity can exist independently in each of the three different directions to form three independent lasers. Point K1 has a unique coupling characteristic unachievable in conventional DFB lasers, the coupling of waves propagating in three different directions as shown in Fig 2.2(b). This means the cavity is a triangular. In fact, there can also be six  $\Gamma$ -K directions in the structure; therefore, two different lasing cavities in different  $\Gamma$ -K directions coexist independently. At point  $\Gamma$  the coupling includes waves in in-plane all six directions;

$0^\circ$ ,  $60^\circ$ ,  $120^\circ$ ,  $-60^\circ$ ,  $-120^\circ$ , and  $180^\circ$  as shown in Fig 2.9c. In addition, the coupled light can be emitted perpendicular from the surface according to first order Bragg diffraction, as shown in Fig 2.3(a). This is the same phenomenon that occurs in conventional grating-coupled surface-emitting lasers. The light wave of band-edges M2, K2 and M3 are also diffraction to an oblique direction vertically. For example, Fig2-3(b) shows the wave-vector diagram of K2 point where the light wave is diffracted to an angle tilted ~~30~~ normally from the sample surface. Fig2-3(c) the wave-vector diagram of one M' point where the light wave is diffracted into three independent angles tilted of about  $22.3^\circ$  and  $51^\circ$  normally from the sample surface, respectively. In these studies, we focus on the folded  $\Gamma_2$  point because of the  $90^\circ$  normally light wave from the sample surface.



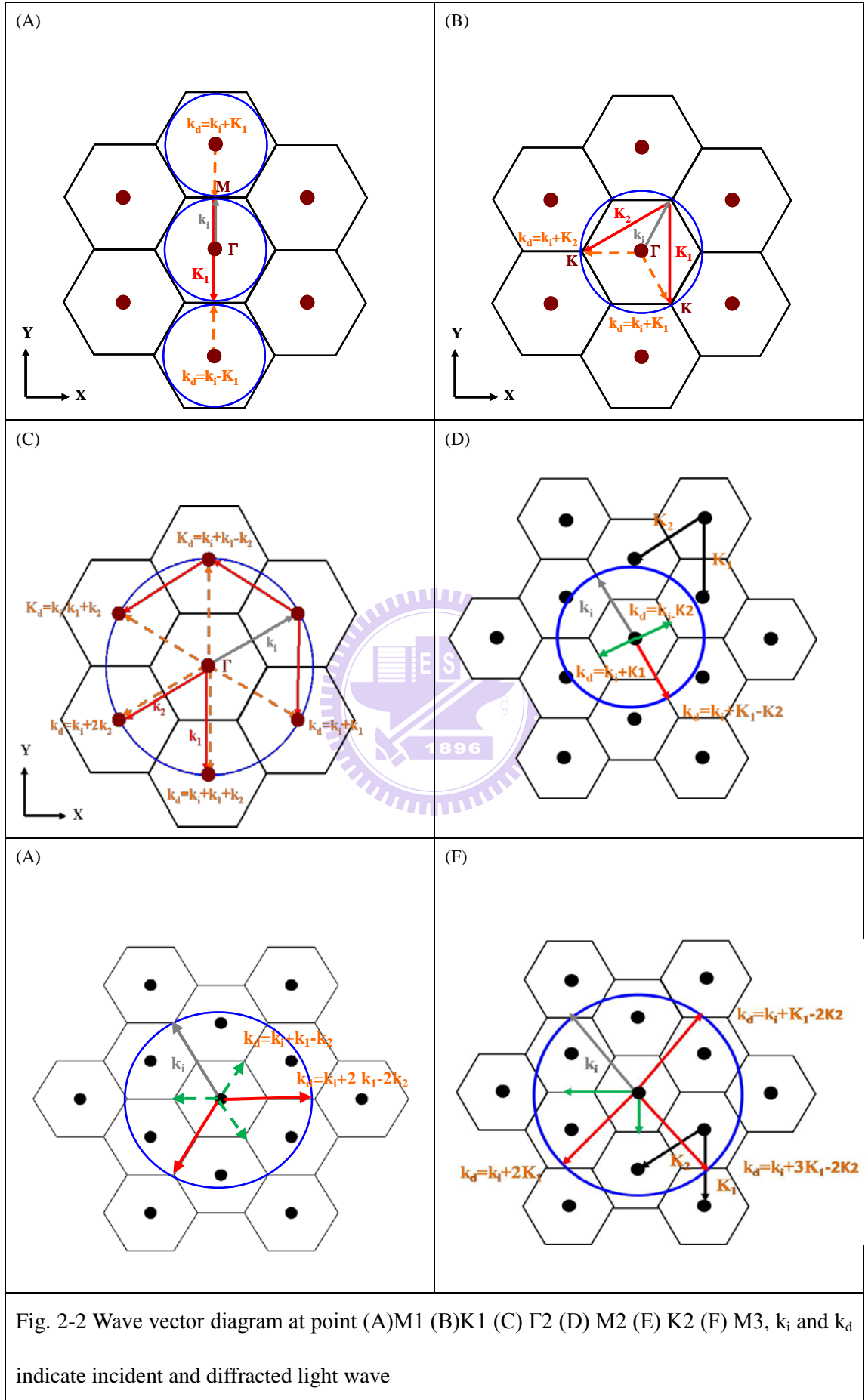
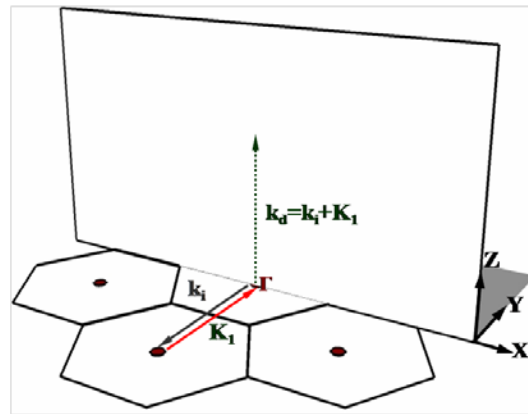
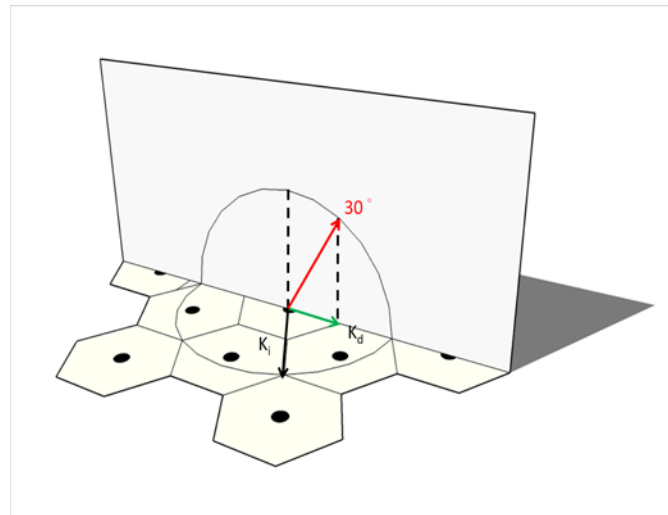


Fig. 2-2 Wave vector diagram at point (A)M1 (B)K1 (C)  $\Gamma_2$  (D) M2 (E) K2 (F) M3,  $k_i$  and  $k_d$  indicate incident and diffracted light wave

(a)



(b)



(c)

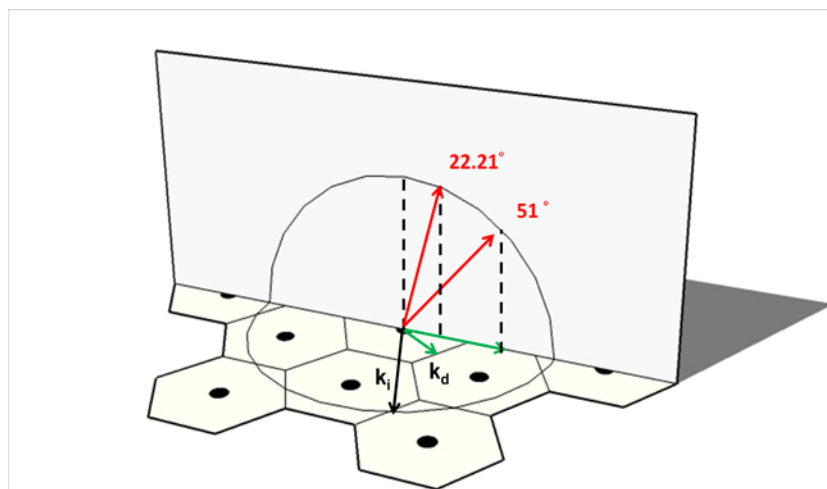


Fig. 2-3 The wave vector diagram at point  $\Gamma$ 2,K2,M3 in vertical direction

## 2.2 Multiple Scattering Method [10-13]

### 2.2.1 2D Gain rod

At first, we consider 2D photonic crystals consist of a triangular lattice with lattice constant  $a$ . A single cylindrical rod (made of gain-creating material A) with radius  $r$  is placed at every lattice point, while the background is made of inactive material B (air). Here, we assume that light is confined in the direction perpendicular to the 2D plane. Let us consider that an optical amplitude gain  $K_a''$  is generated in every rod by either current injection into or optical pumping of all the lattice atoms. This excitation must be done with a sufficient uniformity to guarantee the periodicity of the PC structure. This amplitude gain  $K_a''$  is the negative imaginary part of the complex wave number  $K_a = K_a' - iK_a''$  of light propagating in material A, and therefore the familiar form of gain  $g_a$  (i.e., that for the intensity) is given by  $2K_a''$ . Every rod is assumed to have a constant (i.e.,  $\omega$ -independent) amplitude gain coefficient  $K_a''$  and no loss. We introduce the complex dielectric constant in order to describe the light amplification in the rod:

$$\varepsilon_a(\omega) = \varepsilon_{a0} - i \frac{2c\sqrt{\varepsilon_{a0}}}{\omega} K_a''. \quad (2.3)$$

Here,  $\varepsilon_{a0}$  is the dielectric constant of material A (a real value in the absence of gain). The second term of (2.3) describes the exchange of energy between the electronic and photonic systems.

### 2.2.2 Multiple scattering of light by gain rod array

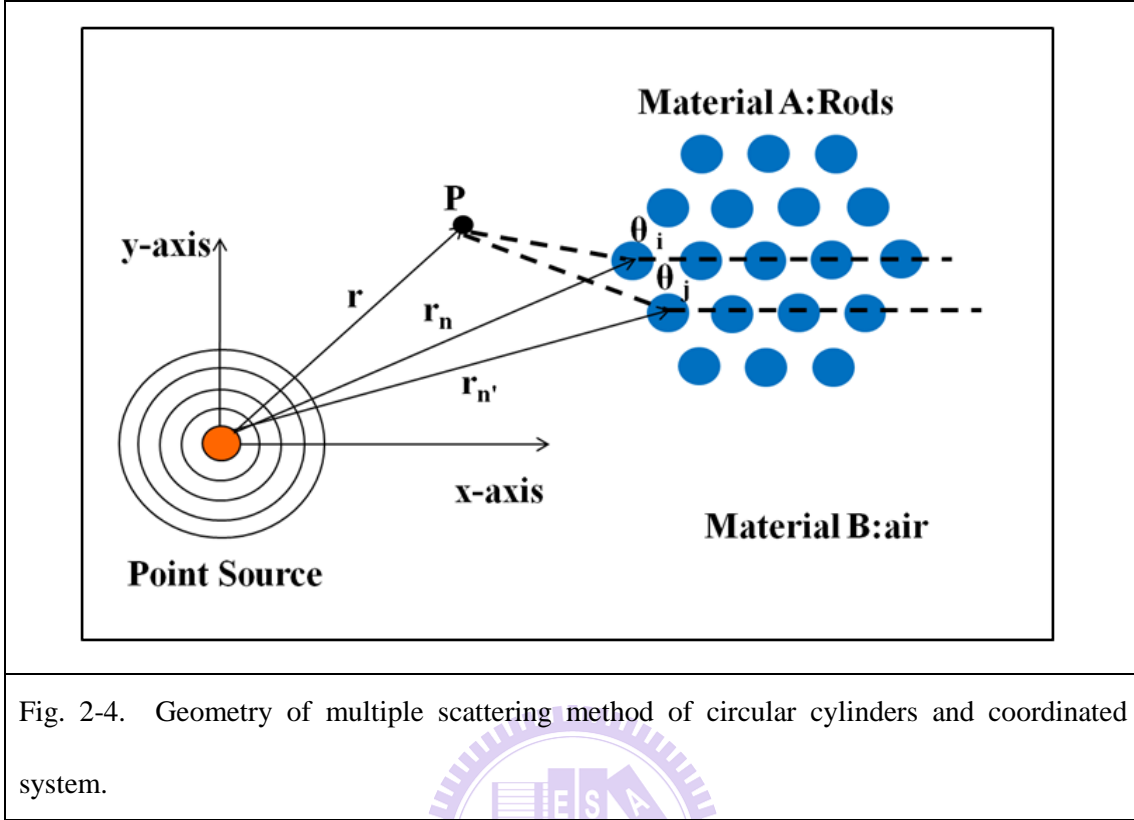


Fig. 2-4. Geometry of multiple scattering method of circular cylinders and coordinated system.

Let us consider a 2D array consisting of finite number ( $N$ ) of cylindrical rods. Here, we focus on the polarization action parallel to the rod axis, which we call the TE mode with the electric-field vector  $\vec{E} = (0, 0, E)$ . Assume that a plane wave with the amplitude  $E_0$  is incident on this array,

$$E^0(\vec{r}) = E_0 e^{i\vec{K} \cdot \vec{r}}. \quad (2.4)$$

Here,  $\vec{K}$  is the wave-number vector  $\vec{K} = (K, \alpha)$  where  $\alpha$  is the incident angle of light and  $K$  is the wave number that is defined in the medium outside all the rods.

Here, we use the 2D generic coordinate  $\vec{r}$  to denote an arbitrary point as viewed from origin  $O$  in the 2D space. First, we focus on the light scattering by a specific rod; e.g.,

the  $n$ th rod. The light wave outside this rod  $E_n^{ex}(\vec{r})$  made up of the wave incident on

this rod  $E_n^i(\vec{r})$  and the wave scattered by this rod  $E_n^s(\vec{r})$ :



$$E_n^{ex}(\vec{r}) = E_n^i(\vec{r}) + E_n^s(\vec{r}). \quad (2.5)$$

Here, the incident wave  $E_n^i(\vec{r})$  on this specific ( $n$  th) rod must contain the incident wave on the array  $E_n^0(\vec{r})$  and the waves scattered by all other rods ( $n'=1,2,\dots,N$ , but  $n \neq n'$ ); i.e.,

$$E_n^i(\vec{r}) = E^0(\vec{r}) + \sum_{n' \neq n} E_{n'}^s(\vec{r}). \quad (2.6)$$

Since  $E_n^s(\vec{r})$  is the wave scattered by the  $n$ th rod, it must have the form of outgoing waves (it never contains incoming components). Therefore, it can be written in the form,

$$E_n^s(\vec{r}) = \sum_{l'=-\infty}^{\infty} b_{n'l'} H_{l'}^{(1)}(Kr_{n'}) e^{il'\theta_{n'}}, \quad (2.7)$$

using the  $l'$  partial-wave expansion, where  $H_{l'}^{(1)}(x)$  is the Hankel function of the first kind which has the asymptotic form of the outgoing wave. Here,  $b_{n'l'}$  is the expansion coefficient and  $r_{n'} \equiv (r_{n'}, \theta_{n'})$  is the polar coordinate as viewed from the center of the  $n$ th rod. As known from (2.6) and (2.7),  $E_n^i(\vec{r})$  is described in terms of a variety of coordinates peculiar to the  $n'$ th rod ( $n \neq n'$ ). It is inconvenient, however, to treat the wavefield containing various different coordinates. So, we transform the expression of (2.7) to the one represented using only the coordinates related to the specific  $n$ th rod  $r_n \equiv (r_n, \theta_n)$ :

$$E_n^s(\vec{r}) = \sum_{l'=-\infty}^{\infty} b_{n'l'} \sum_{l=-\infty}^{\infty} H_{l-l'}^{(1)}(KR_{nn'}) J_l(Kr_n) e^{il\theta_n}. \quad (2.8)$$

In this transformation, we used the addition theorem of Bessel functions. Here,  $R_{nn'}$  is the distance between the centers of the  $n$ th and  $n'$ th rods, and  $\phi_{n'n}$  is the angle that indicates the direction of the  $n$ th rod center as viewed from the  $n'$ th rod center. In a

similar way, it is convenient to transform  $E^0(\vec{r})$  so that it is a function of only the coordinates for the specific  $n$ th rod. By using the relation  $r = R_n + r_n$  ( $R_n$  is the position of the  $n$ th rod center as viewed from the origin),  $E^0(\vec{r})$  can be transformed to

$$E^0(\vec{r}) = \sum_{l=-\infty}^{\infty} a_{nl}^0 J_l(Kr_n) e^{il\theta_n}. \quad (2.9)$$

Here,  $e^{i\vec{K} \cdot \vec{r}_n}$  in (2.4) (note that  $r = R_n + r_n$ ) was expanded using Bessel functions and

$$a_{nl}^0(\vec{r}) = E_0 e^{i\vec{K} \cdot \vec{R}_n} i^l e^{-il\alpha}. \quad (2.10)$$

Now, we rewrite  $E_n^i(\vec{r})$  of Eq. (2.6) as

$$E_n^i(\vec{r}) = \sum_{l=-\infty}^{\infty} a_{nl} J_l(Kr_n) e^{il\theta_n}, \quad (2.11)$$

For simplicity by introducing a coefficient,

$$a_{nl} = a_{nl}^0 + \sum_{n' \neq n} \sum_{l'=-\infty}^{\infty} e^{i(l'-l)\phi_{n'n}} H_{l-l'}^{(1)}(KR_{nn'}) b_{n'l'}. \quad (2.12)$$

which can be obtained by comparing Eq. (2.11) with Eq. (2.6) with the aid of Eqs. (6) and (7). The substitution of Eqs. (2.7) and (2.11) into Eq. (2.5) leads to

$$E_n^{ex}(\vec{r}) = \sum_{l=-\infty}^{\infty} [a_{nl} J_l(Kr_n) + b_{nl} H_l^{(1)}(Kr_n)] e^{il\theta_n}, \quad (2.13)$$

replacing  $n'$  by  $n$  in Eq. (2.7) and  $l$  by in Eq. (2.11). Equation (2.13) is the final form of the light wave outside the  $n$ th rod. This field must be connected to the light wave inside the  $n$ th rod, which can be written as

$$E_n^{in}(\vec{r}) = \sum_{l=-\infty}^{\infty} c_{nl} J_l(K_a r_n) e^{il\theta_n}. \quad (2.14)$$

Note that  $K_a \equiv K'_a - iK''_a$  is the complex wave number defined in the rods, which is assumed to be the same for all rods. For the gain rods considered here,  $K_a \neq 0$ . By imposing Maxwell boundary conditions for the electric field of light at the interface between material A (the  $n$ th rod) and material B (air), we obtain the two relations among the coefficients  $a_{nl}$ ,  $b_{nl}$  and  $c_{nl}$ . By eliminating  $c_{nl}$  from these relations, we get the equation,

$$b_{nl} = s_l a_{nl}, \quad (2.15)$$

Above equation indicates the relation between the two expansion coefficients, then the explicit form of the constant  $s_{nl}$  is given by:

$$s_l = -\frac{KJ'_l(Ka) - \gamma_l J_l(Ka)}{KH^{(1)'}_l(Ka) - \gamma_l H^{(1)}_l(Ka)}, \quad (2.16)$$

Where

$$\gamma_l = -\frac{K_a J'_l(Ka)}{J_l(K_a a)}. \quad (2.17)$$

The expansion  $c_{nl}$  coefficient for the wave inside the  $n$ th rod can be calculated from the boundary conditions at the interface:

$$c_{nl} = \frac{[KH^{(1)'}_l(Ka) - \eta_l H^{(1)}_l(Ka)]}{J_l(K_a a)(\gamma_l - \eta_l)} b_{nl}, \quad (2.18)$$

Where

$$\eta_l = \frac{KJ'_l(Ka)}{J_l(Ka)}. \quad (2.19)$$

The substitution of  $a_{nl}$  from Eq. (2.15) into Eq. (2.12) leads to

$$s_l a_{nl}^0 = b_{nl} - s_l \sum_{n \neq n'} \sum_{l'=-\infty}^{\infty} e^{i(l'-l)\phi_{n'n}} H^{(1)}_{l-l'}(KR_{nn'}) b_{n'l'}. \quad (2.20)$$

This equation is rewritten as a matrix form,

$$T\vec{b} = \vec{q}, \quad (2.21)$$

where  $\vec{b}$  and  $\vec{q}$  are vectors with the elements  $(b_{nl})$  and  $[\vec{q} = (s_l a_{nl}^0)]$ , respectively,

and  $T$  is a matrix, the elements of which are given by

$$T_{nl,n'l'} = \delta_{nn'}\delta_{ll'} - (1 - \delta_{nn'})e^{i(l'-l)\phi_{n'n}}H_{l-l'}^{(1)}(KR_{nn'})s_{l'}, \quad (2.22)$$

where  $\delta$  indicates Kronecker's delta. Since the total scattered wave  $E^s(\vec{r})$  is the sum of light waves scattered by all rods, it can be represented as

$$\begin{aligned} E^s(\vec{r}) &= \sum_n E_n^s(\vec{r}) \\ &= \sum_n \sum_{l'=-\infty}^{\infty} b_{nl'} \sum_{l=-\infty}^{\infty} e^{i(l'-l)\chi_n} J_{l-l'}(KR_n) H_l^{(1)}(Kr) e^{il\theta}, \end{aligned} \quad (2.23)$$

where Eq.(2.7) replacing  $n'$  by  $n$  should be used as  $E_n^s(\vec{r})$  in the middle term rather than another equivalent expression given by Eq. (2.8). Here, in the second equality in Eq.(2.23), used the addition theorem of Bessel functions to transform the  $n$  th rod coordinate  $r_n = (r_n, \theta_n)$  to the generic coordinate  $r = (r, \theta)$ . This transformation is valid only for  $r$  that satisfies  $r \geq R_n$  for all  $n$ . Therefore, Eq. (2.23) holds for light waves scattered toward the outside of the whole rod array.

Note: We assume the point source is more precise for actual optical pumping system, thus we have to modify Eq.(2.4) and Eq.(2.10), the modified coefficients are expressed as:

$$E^0(r) = i\pi H_0^{(1)}(kr) \quad (2.24)$$

$$\begin{aligned} i\pi H_0^{(1)} &= i\pi \sum_{l=-\infty}^{l=\infty} H_{-l}^{(1)}(k|\vec{r}_n|) e^{-il\theta_n} J_l(k|\vec{r}-\vec{r}_n|) e^{-il\phi_{n-n'}} \\ &= \sum_{l=-\infty}^{l=\infty} a_{nl}^0 J_l(k|\vec{r}-\vec{r}_n|) e^{-il\phi_{n-n'}} \end{aligned} \quad (2.25)$$

$$a_{nl}^0(r) = i\pi H_{-l}^{(1)}(k|\vec{r}_n|) e^{-il\theta_n} \quad (2.26)$$

Therefore, we could change the form of the incident wave from plane wave to spherical wave.



## 2.3 Multiple Scattering Method for PCSELs

### 2.3.1 Threshold gain Simulation

The expansion coefficient  $b_{nl}$  in the scattered wave [Eq.(2.23)] is uniquely determined

$$\bar{b} = T^{-1} \bar{q} \quad (2.27)$$

by solving the linear equation Eq. (2.21), when the inverse matrix  $T^{-1}$  exists. Now, let us consider the conditions for laser oscillation in the gain rod array. When there is no incident light wave (i.e.,  $E_0 = 0$ ), we know that  $q=0$ , hence  $b=0$ , and so we obtain no scattered wave:  $E_s = 0$ . Note, however, that there is an exception: if the inverse matrix of  $T$  (i.e.,  $T^{-1}$ ) does not exist, we can observe finite intensity of light even for no light-wave incidence. Or, equivalently, we can obtain an infinitely intense light output even for an incident wave with finite intensity. This is nothing other than a laser oscillation, if it exists. The condition for the nonexistence of  $T^{-1}$ , i.e.,

$$\det(T) = 0, \quad (2.28),$$

can be regarded as the laser oscillation condition in our case.

Since matrix  $T$  is a complex function of both the optical frequency through  $K = \omega / c$  and the amplitude gain  $K_a$  through Eq.(2.3), we can obtain mode frequency  $\omega_m$  and threshold amplitude gain  $K_{am}$  for the laser oscillation by searching for the pair of variables ( $\omega$  and  $K_a$ ) at which the determinant for  $T$  vanishes. Fig. 2-5 shows the results by searching for the pair of variables ( $\omega$  and  $K_a$ ). The x-axis represents amplitude gain, y-axis represents normalized frequency and z-axis means inverse value of determinant for  $T$  matrix. It is obvious that lasing mode show up at which the inverse determinant value for divergent points.

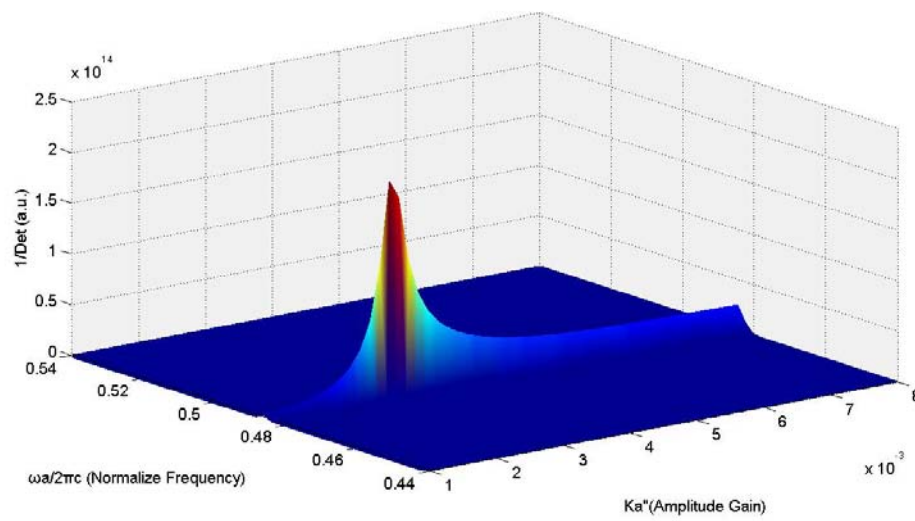


Fig. 2-5 The peak is indicated the normalized frequency and threshold amplitude gain  $K_{am}^*$  at the calculated lasing modes.



### 2.3.2 Resonant Mode Simulation

To investigate the features of light waves within the PCSELS, we try to figure out the mode patterns of PC. At first, we find out the lasing PC mode after we search the pair of variables ( $\omega$  and  $K_a$ ) from Eq. (2.28), then we apply variables into the Eq. (2.23) to obtain the electric field  $E_z(r)$ . The electric field  $E_z(r)$  could give us the great information to classify different lasing modes at band edge. Moreover, to investigate more precisely what occurs within the PCs, we calculate the Poynting-vector distributions in the PCs immediately before the onset of laser oscillation. The definition of Poynting-vector is:

$$\vec{S}(\vec{r}, t) = \frac{c_0}{4\pi} \vec{E}(\vec{r}, t) \times \vec{H}(\vec{r}, t), \quad (2.29)$$

Then, the time-average Poynting-vector is written as:

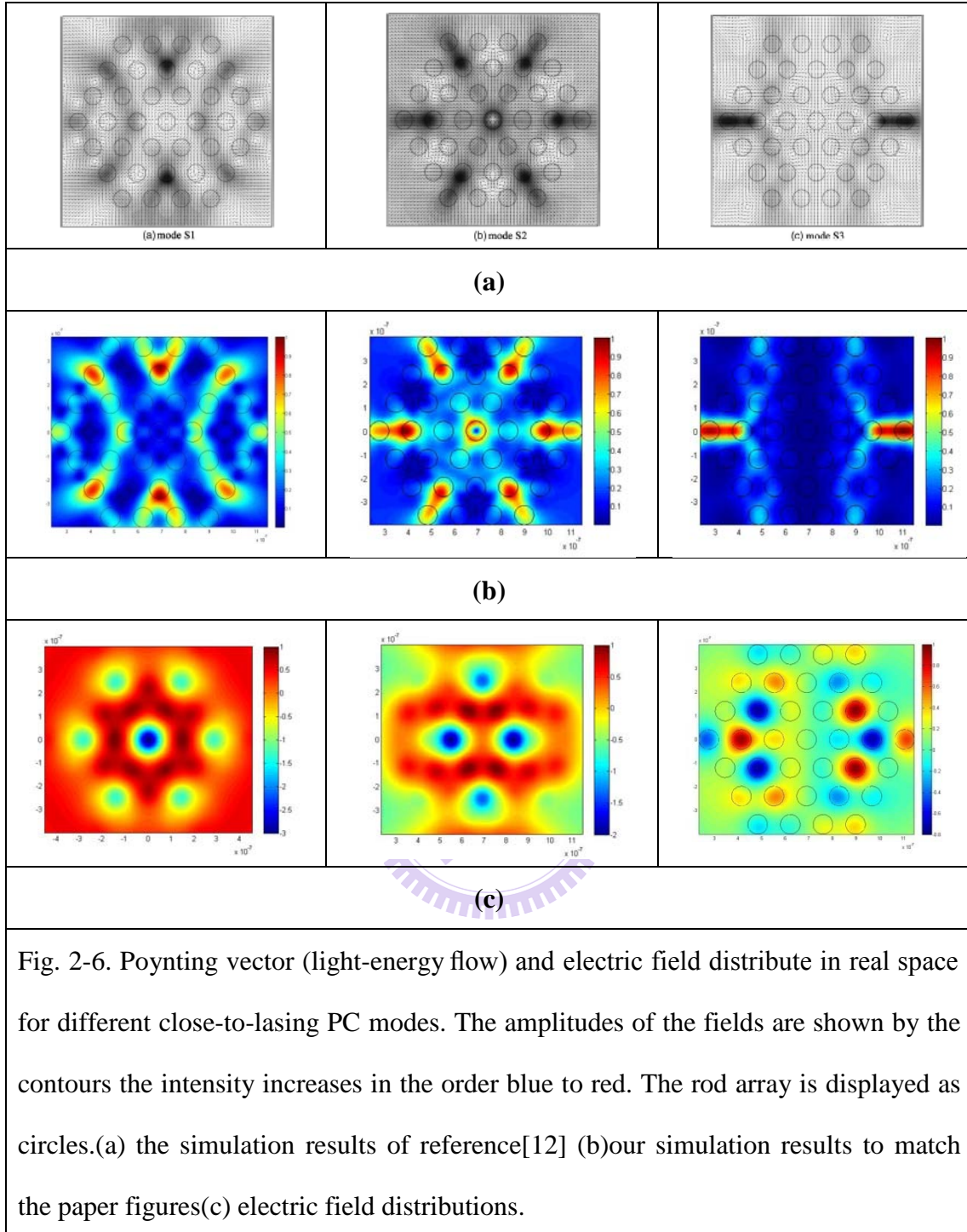
$$\vec{P}_{av} = \frac{c_0}{8\pi} \text{Re}\{\vec{E} \times \vec{H}^*\} \quad (2.30)$$

Since the Poynting vectors represent the light-energy flux, their results will vividly demonstrate the behaviors of light in the PCs.

As a result, we show the results of the electric field and Poynting-vector in Fig. 2-6.

\





### 2.3.3 Reciprocal space (K-Space) Simulation

People always transfer the data in time-domain to frequency-domain because it is easier to explain some physical mechanisms in frequency-domain than time-domain.

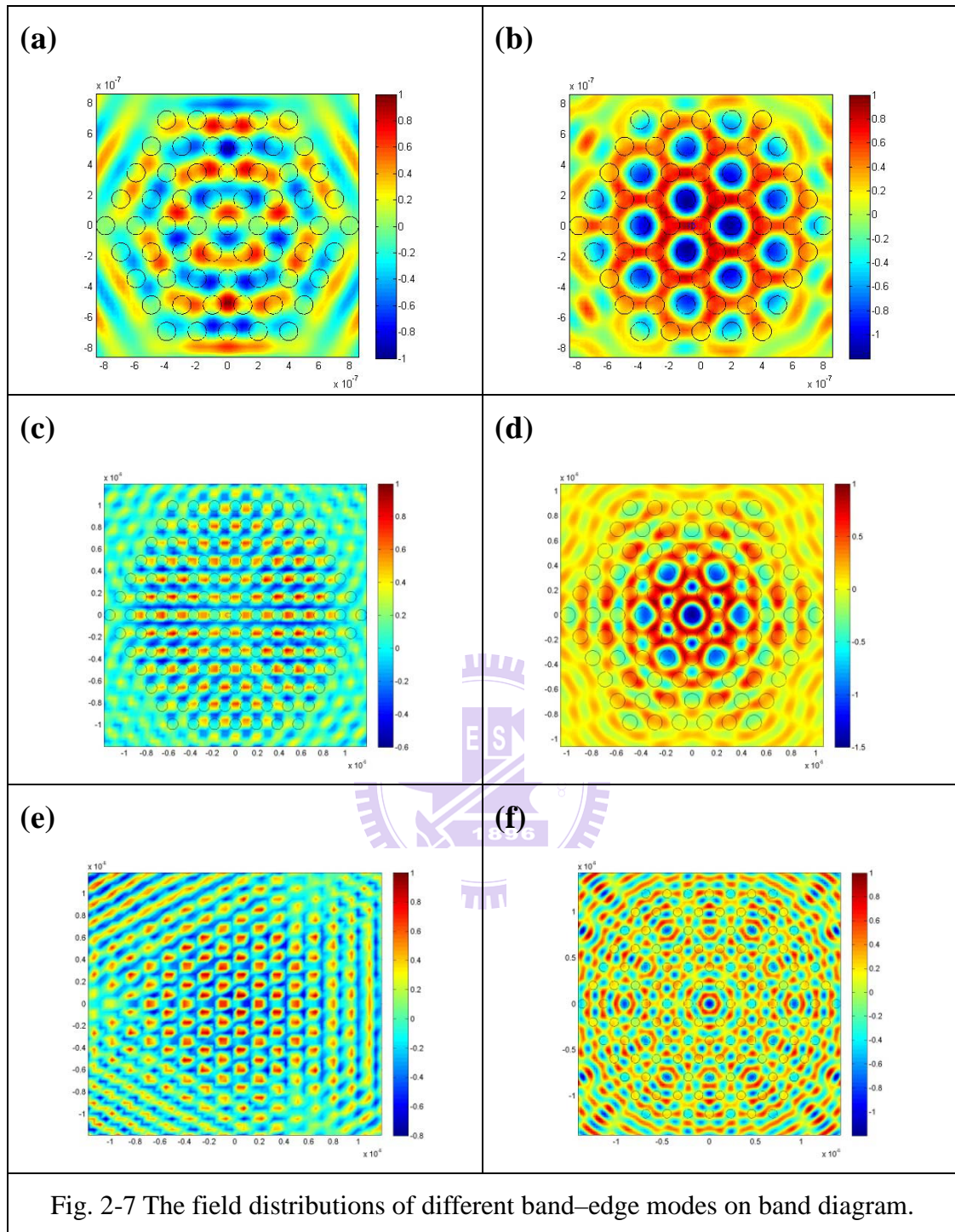
Here, we use the Fast Fourier Transform (FFT) method to calculate the field-intensity spectra in reciprocal space (K-space). We transform the Eq. (2.23) into reciprocal lattice space by FFT, then, the mode distribution in reciprocal space is calculated as:

$$E(\vec{g}) = \int_{|\vec{r}| < \infty} E(\vec{r}) e^{-i\vec{g} \cdot \vec{r}} d\vec{r} \quad (2.31)$$

The mode distribution in reciprocal space would illustrate the oscillation condition at different band edge point of band diagram. Fig. 2-7 shows the electric field distributions near different band-edge points. Fig. 2-8 is obtained by the Fourier transform of the field of the PC area in Fig. 2-7. The K-space that calculated by the 2D Multiple Scattering Method distributions are consistent with the Bragg diffraction as discussed in section 2-1, indicating that the resonant field distributions are caused by band edge resonance.

The black circles represent the photonic crystal air hole and the intensity of electric field are distributed from blue to red. We normalized the intensity to 1. The white hexagonal in Fig. 4-8 represents the Brillouin zone with different lattice points.

The pattern of Fig. 4-7(a) and Fig. 4-8(a) indicates that the mode is caused by the resonance at the M1 point. As the results of section 2-1, we demonstrate resonant mode pattern and K-space simulation by multiple scattering for whole band-edge points.



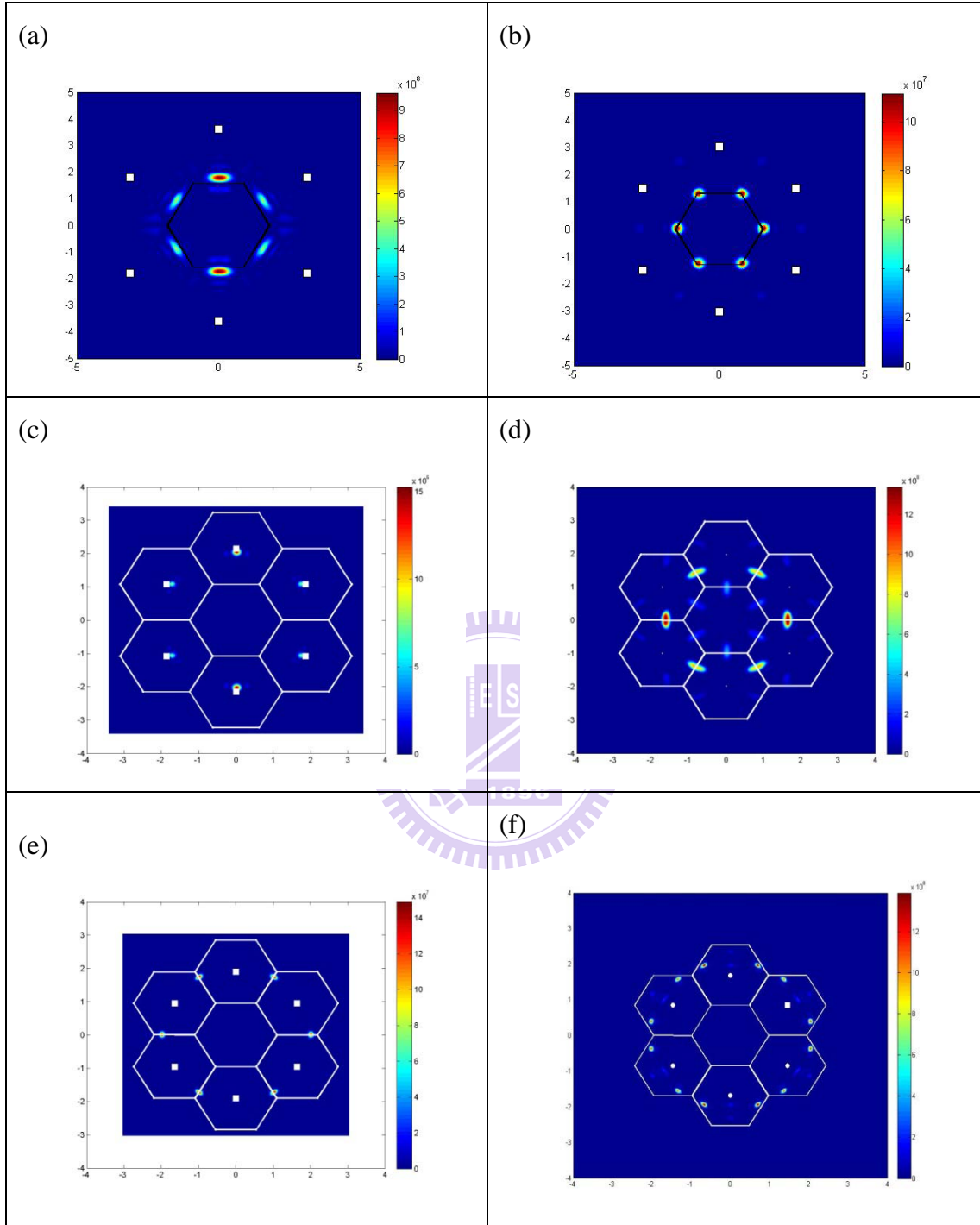


Fig. 2-8 The K-space distributions of different band-edge modes for PCSEL.

These are used Fast Fourier Transform method by Eq (2.31)

## Reference

- [1] M. Imada, S. Noda, A. Chutinan, T. Tokuda, M. Murata, and G. Sasaki, Appl. Phys. Lett. 75, 316 (1999)
- [2] S. Noda, M. Yokoyama, M. Imada, A. Chutinan, and M. Mochizuki, Science 293, 1123 (2001)
- [3] H. Y. Ryu, S. H. Kwon, Y. J. Lee, and J. S. Kim, Appl. Phys. Lett. 80, 3467 (2002)
- [4] G. A. Turnbull, P. Andrew, W. L. Barns, and I. D. W. Samuel, Appl. Phys. Lett. 82, 313 (2003)
- [5] K. Sakai, E. Miyai, T. Sakaguchi, D. Ohnishi, T. Okano, and S. Noda, IEEE J. Sel. Areas Commun. 23, 1335-1340 (2005)
- [6] M. Imada, A. Chutinan, S. Noda and M. Mochizuki Phys. Rev. B 65, 195306 1-8 (2002)
- [7] M. Yokoyama and S. Noda Opt. Express 13, 2869-2880 (2005)
- [8] M. Imada, A. Chutinan, S. Noda, M. Mochizuki, Phys. Rev. B, 65, 195306 (2002)
- [9] M. Notomi, H. Suzuki, and T. Tamamura, Appl. Phys. Lett., 78, 1325 (2001)
- [10] S. Nojima, Appl. Phys. Lett., 79, 1324 Sep (2001)
- [11] S. Nojima, J.J. Appl. Phys., 38, L867-L869 Aug (1999)
- [12] S. Nojima Journal of Appl. Phys 98, 043102 (2005)
- [13] S. Nojima Phys Review B, 65, 073103,(2002)

# Chapter 3

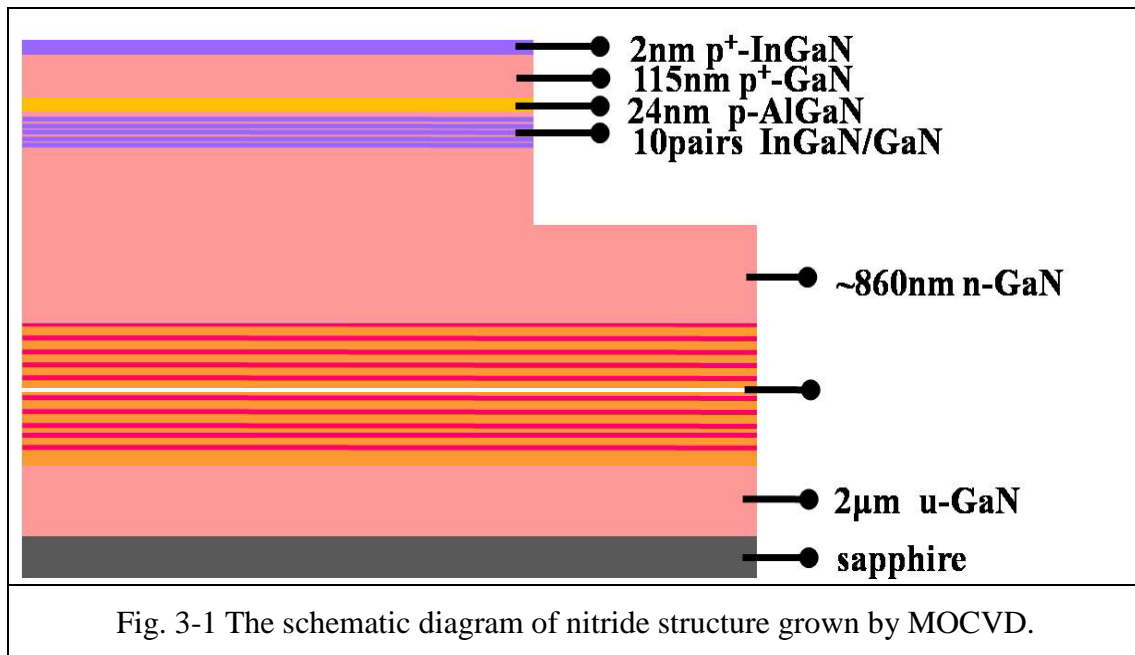
## Fabrication of GaN-based 2D Photonic Crystal

### Surface Emitting Lasers

#### 3.1 Wafer Preparation

The GaN-based heterostructure of MCLED was grown by metal-organic chemical vapor deposition (MOCVD) system (EMCORE D-75) on the polished optical-grade c-face (0001) 2" diameter sapphire substrate, as shown in Fig 3-2. Trimethylindium (TMIn), Trimethylgallium (TMGa), Trimethylaluminum (TMAI), and ammonia (NH<sub>3</sub>) were used as the In, Ga, Al, and N sources, respectively. Initially, a thermal cleaning process was carried out at 1080°C for 10 minutes in a stream of hydrogen ambient before the growth of epitaxial layers to clean the sample surface. Second, the 30nm thick GaN nucleation layer was first grown on the sapphire substrate at 530°C, and then 2μm thick undoped GaN buffer layer was grown on it at 1040°C. After that, a 29 pairs of quarter-wave GaN/AlN structure was grown at 1040°C under the fixed chamber pressure of 100Torr and used as the high reflectivity bottom DBR. Finally, the 7λ active pn-junction region was grown atop the GaN/AlN DBR, composed typically of ten pairs In<sub>0.2</sub>Ga<sub>0.8</sub>N quantum wells (LW=2.5 nm) with GaN barriers (LB=7.5 nm), surrounded by 560nm thick Si-doped n-type GaN layer, and 200nm thick Mg-doped p-type GaN layers.





### 3.2 Process Procedure

There are some principles to fabricate GaN-based PCSELs, including initial clean (I.C.), plasma enhanced chemical vapour deposition (PECVD) technique, EBL technique and inductively coupled plasma - reactive ion etching (ICP-RIE) technique. The purpose of the I.C. is to remove the small particle and organism on the sample surface. The steps of I.C. are described as below.

#### Initial clean (I.C.)

1. Degreasing particles in acetone (ACE) 5min by ultrasonic baths.
2. Dipping in isopropyl alcohol (IPA) 5min by ultrasonic baths for organism removed.
3. Rising in de-ionized water (D.I. water) 5min for surface clean.
4. Blowing with N<sub>2</sub> gas for surface drying.
5. Baking by hot plate 120°C, 5min, for wafer drying.

#### PECVD (SAMCO PD220)

The purpose of PECVD technique is to deposit a SiN film for hard mask. The details of PECVD parameters are expressed as below.

1. Initial clean
2. SiN film deposition: SiH<sub>4</sub>/Ar : 20sccm  
NH<sub>3</sub>: 10sccm  
N<sub>2</sub>: 490sccm  
Temperature: 300°C  
RF power: 35W  
Pressure: 100Pa  
Time: 20min for depositing SiN 200nm



### E-Beam Lithography (EBL)

The purpose of the EBL is to define the PC pattern on the photoresist (PMMA) (soft mask). In the process of EBL, a special positive photoresist PMMA (A5) was used. These EBL parameters are described as below.

1. Spin coating use the photoresist : PMMA (A5).
  - a. first step: 1000 rpm for 10sec.
  - b. second step: 5000 rpm for 90sec.
2. Hard bake: hot plate 180°C, 1hr.
3. Exposure :  
Beam voltage: 10KeV  
Writefield size: 50μm
4. Development: dipping in IPA : MIBK(3 : 1) 50sec.
5. Fixing: rising in IPA 30sec.
6. Blowing with N<sub>2</sub> gas for drying.
7. Hard bake: hot plate 120°C, 4min.

### ICP-RIE (Oxford Plasmalab system 100)

The soft mask was transferred to SiN film to form the hard mask by using ICP-RIE. These ICP-RIE techniques are described as below.

1. SiN film etching:  
Ar/O<sub>2</sub>: 5sccm  
CHF<sub>3</sub>: 50sccm  
Forward power: 150W  
Pressure: 7.5\*10<sup>-9</sup>Torr  
Temperature: 20°C  
Time: 100 second for etching SiN film 200nm
2. Initial clean for remove soft mask

### ICP-RIE (SAMCO RIE-101PH)

The purpose of the ICP-RIE technique is to form the PC layer on GaN. The hard mask was transferred to GaN by using ICP-RIE technique. Fig 3-2 shows the SEM image of top view and cross section of completed 2D PCSELS, respectively. These ICP-RIE techniques are described as below.

1. P-GaN etching:

Ar: 10sccm

Cl<sub>2</sub>: 25sccm

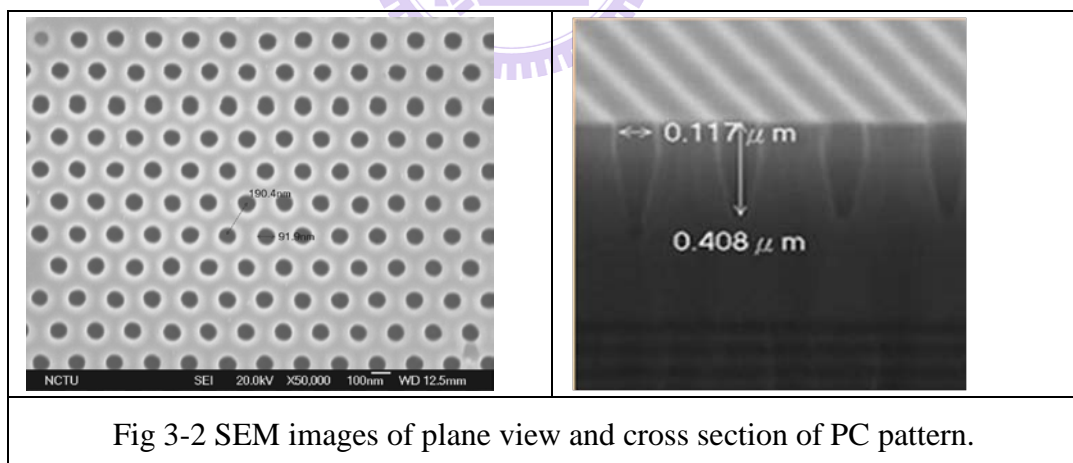
ICP power: 200W

Bias power: 200W

Pressure: 0.33Pa

2. Dipping BOE 40sec. for remove hard mask

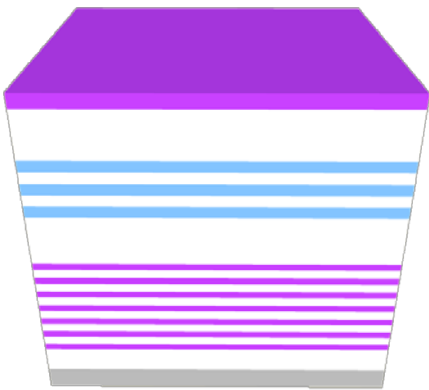

3. Polishing sapphire for optical pumping



### 3.3 Process flowchart

The PCSELS was fabricated by following process steps. In the beginning, the hard mask SiNx 200nm was deposited by PECVD. Then PMMA layer (300nm) was spun by spinner and exposed using E-beam writer to form soft mask. The pattern on soft mask was transferred to SiNx film to form the hard mask by using ICP-RIE (Oxford Plasma lab system 100), and then the PMMA layer was removed by dipping ACE. The pattern on hard mask was transferred to GaN by using ICP-RIE (SAMCO RIE-101PH) to form the PC layer. Finally, the sample dips in BOE to remove the hard mask. Fig. 3-5 shows the process of flow chart of PCSEL.



(a) SiNx film	(b) PMMA
	

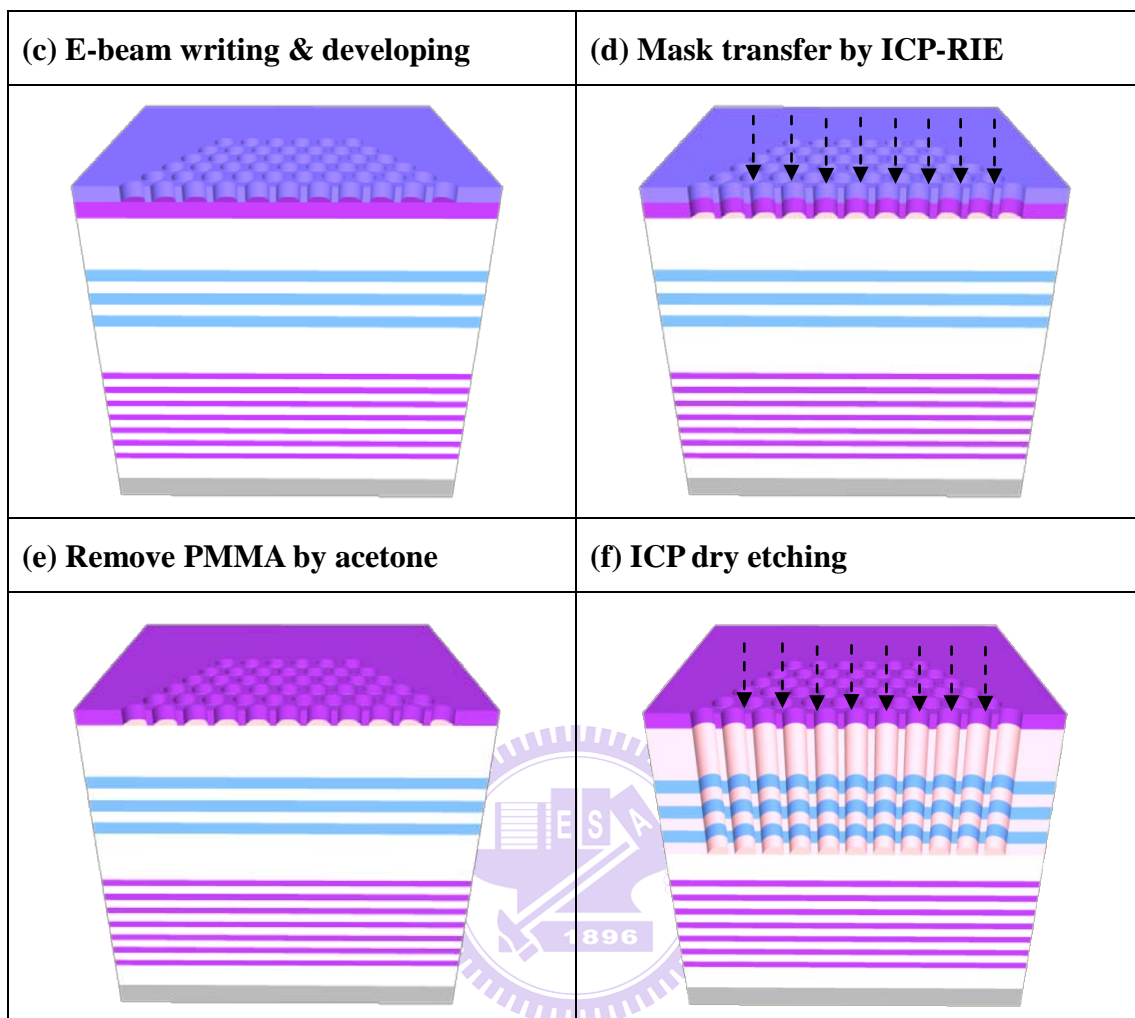


Fig. 3-3 Process flow chart of PCSELS, steps are ordered from (a) to (f).

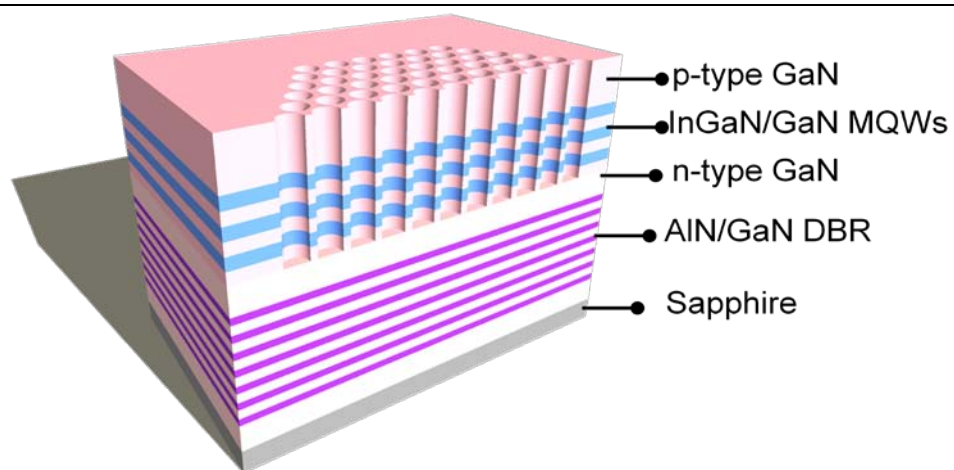


Fig. 3-4 Complete PCSELS' device after removing SiNx film.

To completely describe the process flowchart, each process conditions are entirely listed in the table.

<b>Step</b>	<b>Process</b>	<b>Conditions</b>
<b>1</b>	<b>Soft mask</b>	<b>Initial clean(I.C.)</b> <b>(2) Deposit 200nm SiNx by PECVD.</b> <b>(3) Spin 150nm PMMA by spinner.</b> <b>(4) Define PCSELS pattern by EBL.</b> <b>(5) Development.</b> <b>(6) Hard bake</b>
<b>2</b>	<b>Hard mask</b>	<b>(1) Dry etching by ICP-RIE (Oxford Plasmalab system 100) to form the hard mask.</b> <b>(2) Remove PMMA by ACE.</b> <b>(3) Hard bake.</b>
<b>3</b>	<b>PCSELS</b>	<b>(1) Dry etching by ICP-RIE ((SAMCO RIE-101PH) to transfer the hard mask to GaN.</b> <b>(2) Remove hard mask by BOE.</b> <b>(3) Hard bake.</b>

# Chapter 4

## Simulation and Experiment Results of GaN-based 2D Photonic Crystal Surface Emitting Lasers

### 4.1 The design for PCSEL

In this section, we focus on the design parameters of simulation for our GaN-based PCSELS. As usual, we calculate the dispersion band diagram to determine the normalized frequency which we choose for specific band-edge groups by PWEM. Then, we calculate the more accurate threshold gain and normalized frequency by multiple scattering method (MSM). Normalized frequency is the ratio of the lasing wavelengths of optical modes and the PC lattice constants. Once the lasing wavelength is determined, the lattice constant is certain to be determined. The lasing wavelength is located within the emission of the active layer. According to the theory described in chapter 2, the surface emitting laser in the photonic crystal grating structure could only happen as the Bragg condition is satisfied. In fact, the 2-D PWEM and MSM couldn't precisely evaluate the photonic band diagram and threshold gain for our 3-D structure. That means we should do some modification to parameters describing our structure and then bring them into the 2-D PWEM and MSM to approximate real condition. Therefore, we bring two parameters including confinement factor ( $\Gamma_g$ ) and effective refractive index ( $n_{\text{eff}}$ ) into our calculation.  $\Gamma_g$  is the ratio of the light field confined within the 2-D PC structure to the light inside the whole device, and  $n_{\text{eff}}$  is the effective refractive index of the entire device with PC that take into account the effects of partial modal overlap of electromagnetic fields.  $\Gamma_g$  and  $n_{\text{eff}}$  could be used to estimate the effective dielectric constant of nano-hole ( $\epsilon_a$ ) and the background ( $\epsilon_b$ ) for 2-D calculation to further approximate the 3-D structure. These two parameters can be obtained by solving the distribution of the electric field in the

in-plane direction. It is first estimated by transfer matrix method and shown in Fig 4-1.

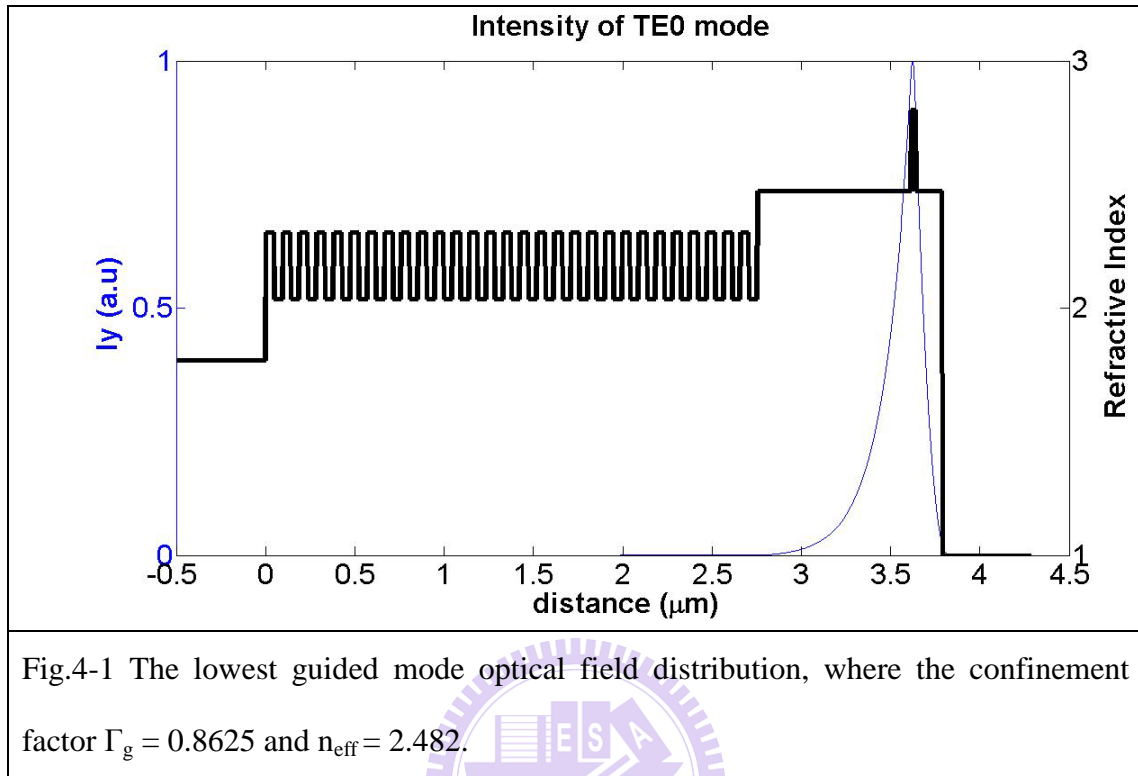


Fig.4-1 The lowest guided mode optical field distribution, where the confinement factor  $\Gamma_g = 0.8625$  and  $n_{\text{eff}} = 2.482$ .

The  $\Gamma_g$  and  $n_{\text{eff}}$  for describing our structure are estimated to be 0.8625 and 2.482 considering fundamental mode, respectively.

Then, we could determine  $\epsilon_a$  and  $\epsilon_b$  using two conditions:

$$\begin{cases} n_{\text{eff}}^2 = f\epsilon_a + (1-f)\epsilon_b \\ \Delta\epsilon = \epsilon_b - \epsilon_a = \Gamma_g(\epsilon_{\text{mat}} - \epsilon_{\text{air}}) \end{cases} \quad (4-1)$$

where the  $f$  is air filling factor,  $\epsilon_{\text{mat}}$  is the dielectric constant of semiconductor, and  $\epsilon_{\text{air}}$  is the dielectric constant of air. For a triangular lattice PC,  $f$  is written as:

$$f = \frac{2\pi r^2}{\sqrt{3}a^2} \quad (4-2)$$

Therefore, the value of  $\epsilon_a$  and  $\epsilon_b$  in unit cell for our PC device could be obtained the values are about 4.11 and 7.07, respectively. To bring  $\epsilon_a$  and  $\epsilon_b$  into the calculation, a band diagram of the 2-D PC structure with triangular lattice for TE-like mode with  $r/a = 0.28$  on our sample structure could be estimated as shown in Fig 4-2. The figure shows that the dispersion curve of each mode would cross and splits at specific band-edges, and the mode density is higher at those boundaries. Light at these areas can propagate along different direction and have chance to couple and form a laser cavity.

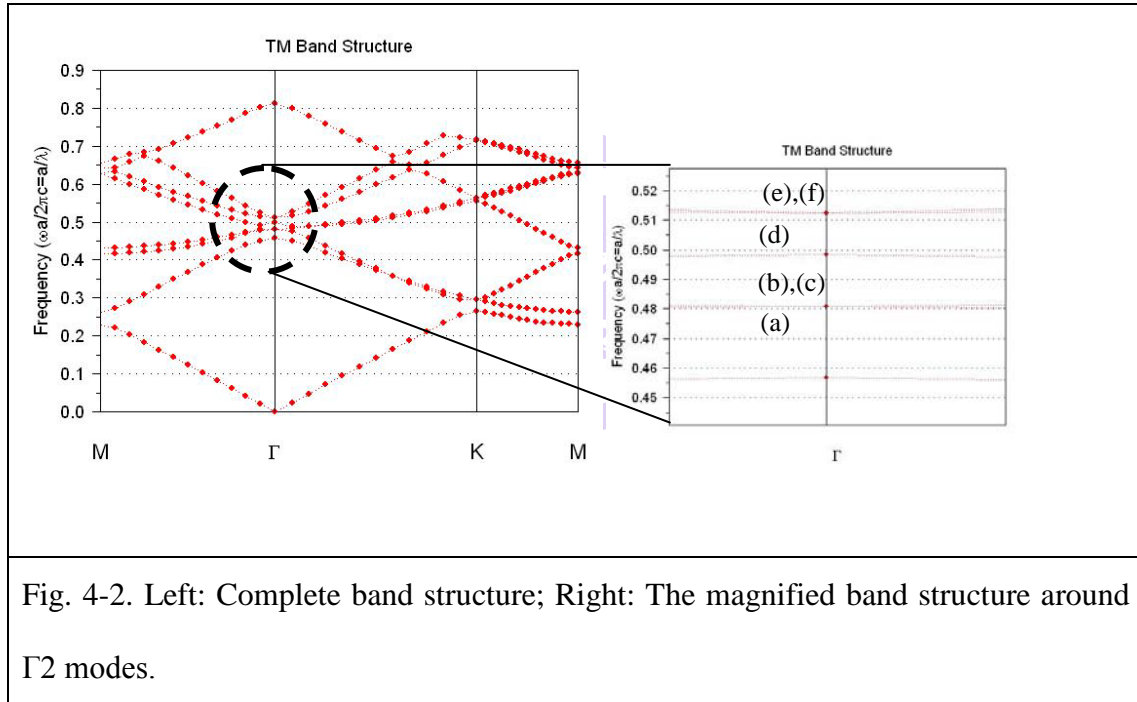


Fig. 4-2. Left: Complete band structure; Right: The magnified band structure around  $\Gamma_2$  modes.

The calculated band diagram in the vicinity of  $\Gamma_2$  is shown in right of Fig. 4-2. There are six bands, resulting from the six coupling waves. There are two pairs of doubly degenerate bands and two pairs of non-degenerate bands. We will call these bands (a), (b), (c), (d), (e) and (f), as indicated in Fig. 4-2; bands A and C are non-degenerate and bands B and D are doubly degenerate. The electromagnetic field distribution in the plane of the photonic crystal plane calculated for each mode by the multiple scattering



method is shown in Fig. 4-3. Fig. 4-3(a)–4-3(f) correspond to bands (a)–(f), respectively. The amplitudes of magnetic field in the direction perpendicular to the plane are indicated by the red and blue areas, corresponding to positive and negative amplitudes, respectively.

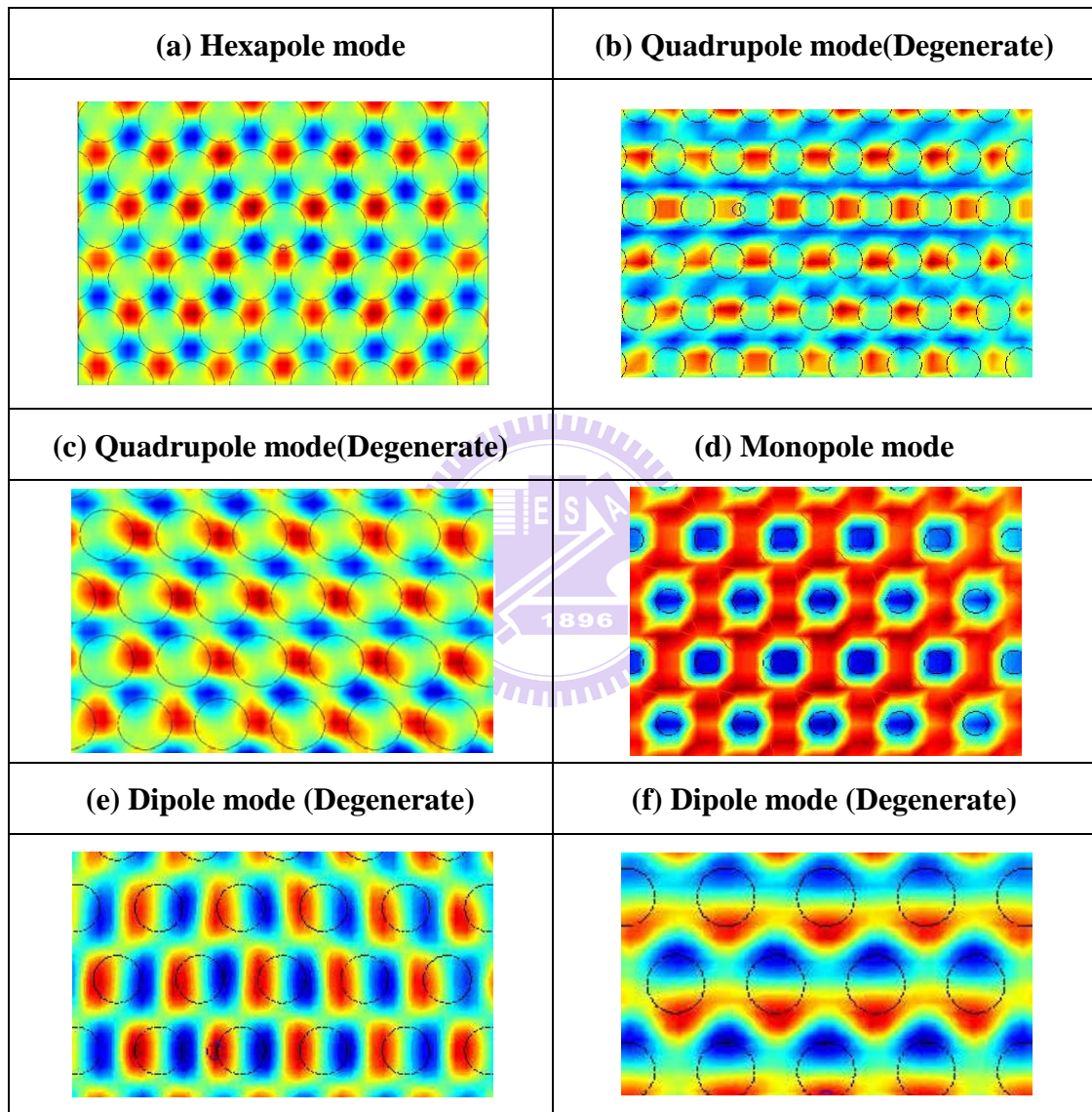


Fig. 4-3 (a)-(f) are the magnetic field distributions of six modes in Fig 4-2 .Blue and red areas correspond to positive and negative magnetic fields perpendicular to the plane. Black circles indicate lattice points.

## 4.2 The effect of Photonic Crystal Shell [1]

In this section, the multiple scattering method is used to calculate the general features of band edge effect such as threshold gain and wavelength. The threshold gain and normalized frequency would shift to band edge as increasing the shell number of photonic crystals. As mentioned in section 4-1, the transfer matrix method is calculated to obtain the value of  $\epsilon_a$  and  $\epsilon_b$  in unit cell for our PC device. Therefore, we could obtain the values of  $\epsilon_a$  and  $\epsilon_b$  about 4.11 and 7.07. Here, we introduce a size parameter  $N$  that means the number of air-hole layers in the  $\Gamma$ -M direction. For example,  $N$  is 7 in the calculation domain of Fig 4-4. This domain contains 37 air holes. The horizontal dash line in Fig 4-4 corresponds to the band-edge frequency of the infinitely-size structure that calculated from PWEM. The value of the normalized frequency would approach the band-edge position as  $N$  increases. Here, we observed the normalized frequency of the  $\Gamma_2$  peak would decreases with  $N$  in Fig 4-4. These results are related to the shape of the band that we discussed is located at the local maximum of the band. Therefore, infinite-size structure, the frequency should mainly be distributed above the  $\Gamma_2$  band edge and approach that band-edge point as the structure size increases. Next, threshold gain are calculated as a function of  $N$  for the  $\Gamma_2$  points and plotted in Fig 4-5. As expected, threshold gain values generally decrease with  $N$ . However, the decreasing behavior is not as linear as we predict, the slope of threshold gain will slower down as  $N$  increase. The possibly reason is that the effect of photonic crystal shell is decreased with  $N$  number. Therefore, the threshold gain would exponential decay as shell number increase.

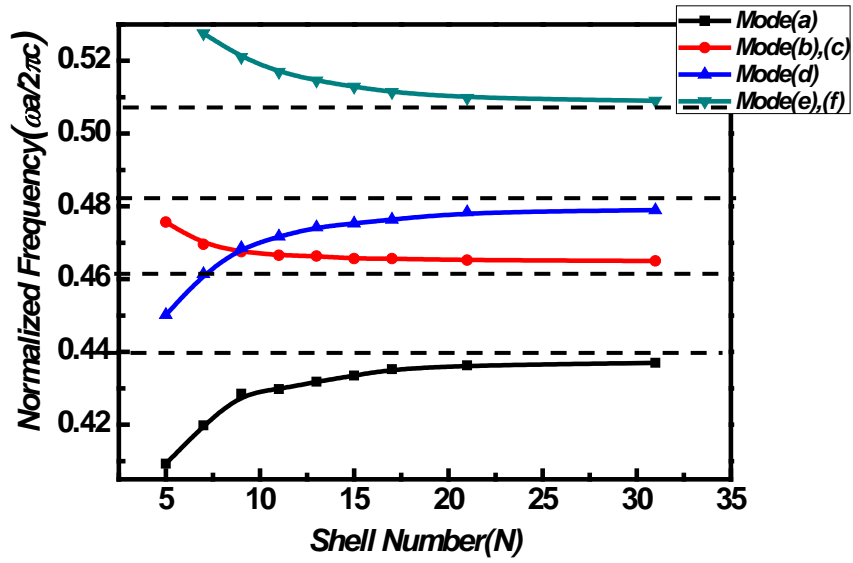


Fig. 4-4. Normalize frequency would shift near band edges for different PC Shell ( $N$  values). The horizontal dash line indicates the normalized frequency of band edge calculated by PWEM.

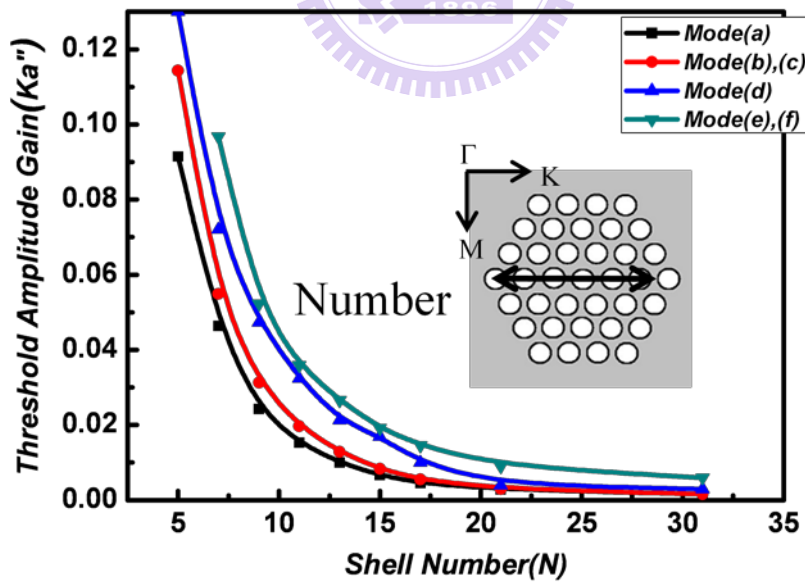


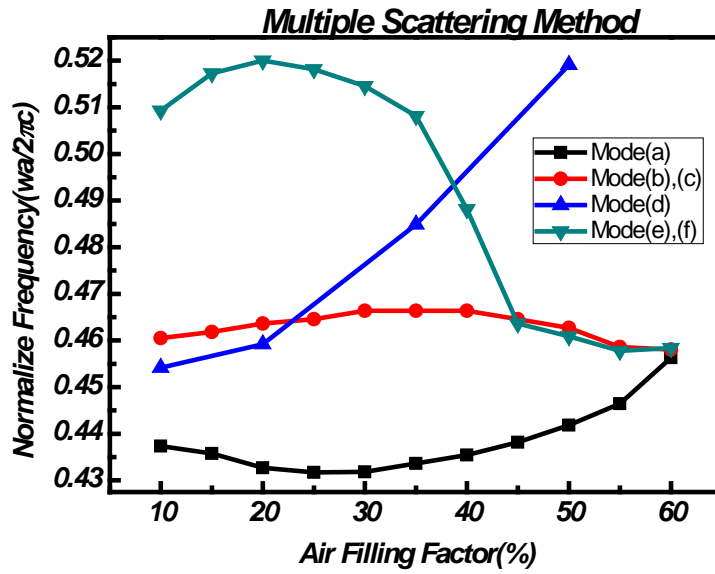
Fig. 4-5. Threshold gain as a function of the number of air-hole layers ( $N$ ) for  $\Gamma_2$  band-edge resonance of a 2D photonic crystal.

### 4.3 The effect of Photonic Crystal Filling Factor [2-4]

In this part, we will investigate the effect of filling factor for PCSEL. As the section 4-1, we have to consider the effective refractive index when we use different filling factor. Here, the effective refractive index values are given in the Appendix. In Fig. 4-6(a) we present the resonant mode frequencies as a function of the filling factor, using the resonant mode patterns and k-space distribution to classify. The corresponding frequencies calculated using the 2D PWEM are shown in Fig. 4-6(b). The two sets of results are in good agreement; the minor deviations are due to the N number used in each method. We used  $N=13$  to determine the resonant mode frequencies in 2D MSM, while N number is infinitely-size used in the 2D PWEM.



(a)



(b)

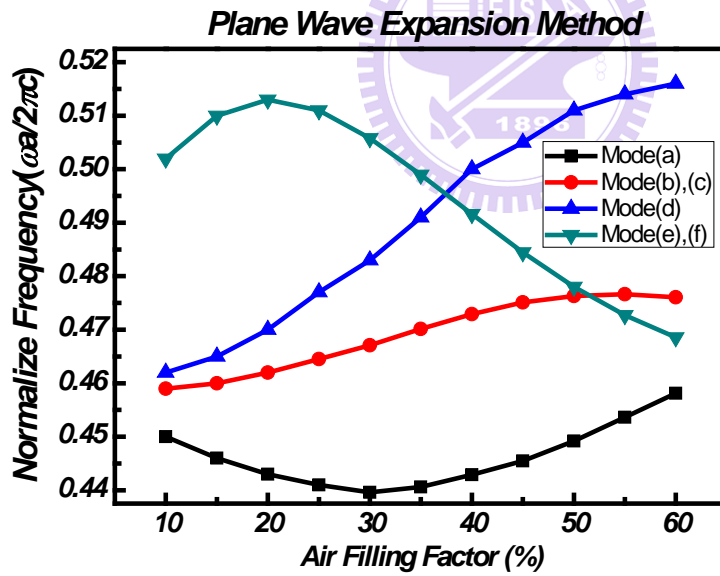


Fig. 4-6. Normalized resonant mode frequencies as a function of the filling factor, calculated using (a) the Multiple Scattering Method, and (b) the 2D PWEM

Next we investigate the dependence of threshold gain on the hole-filling factor. Fig 4-7 plots the threshold gain of the modes (a) ~ (f) as functions of the air-filling factor. The black curve is represented the threshold gain of hexapole mode, the red curve represents quadrupole mode (the dipole mode is a degenerate mode) and blue and green curves represent monopole mode and dipole mode (degenerate mode), respectively.

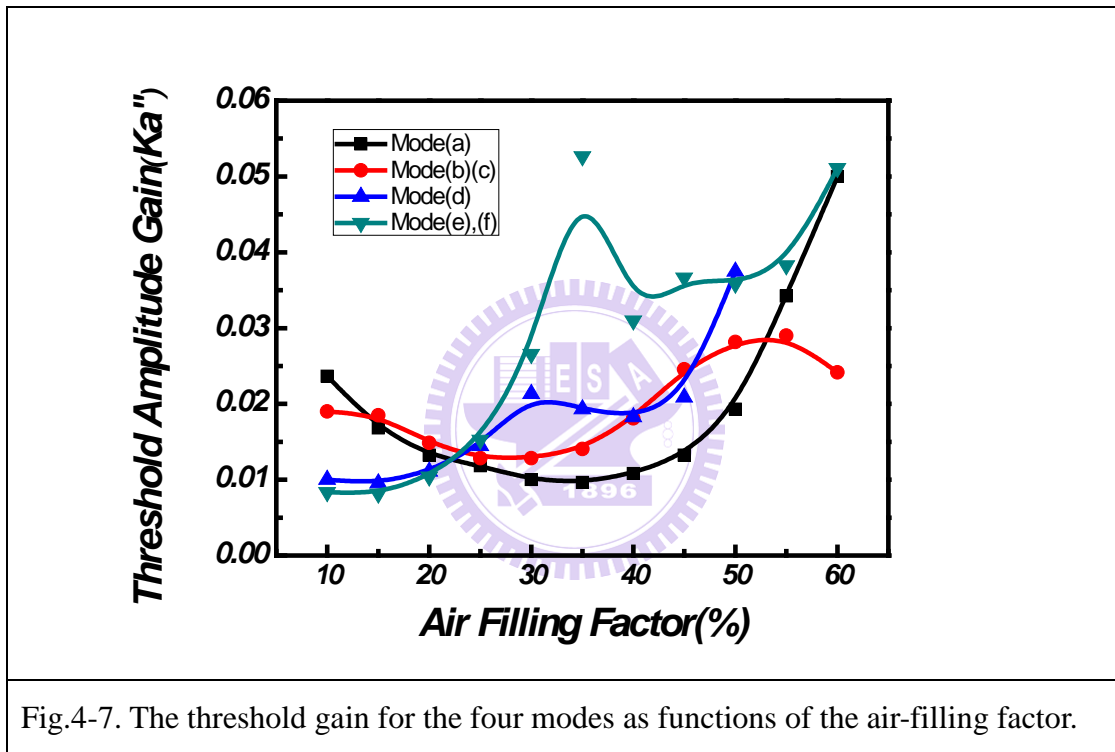


Fig.4-7. The threshold gain for the four modes as functions of the air-filling factor.

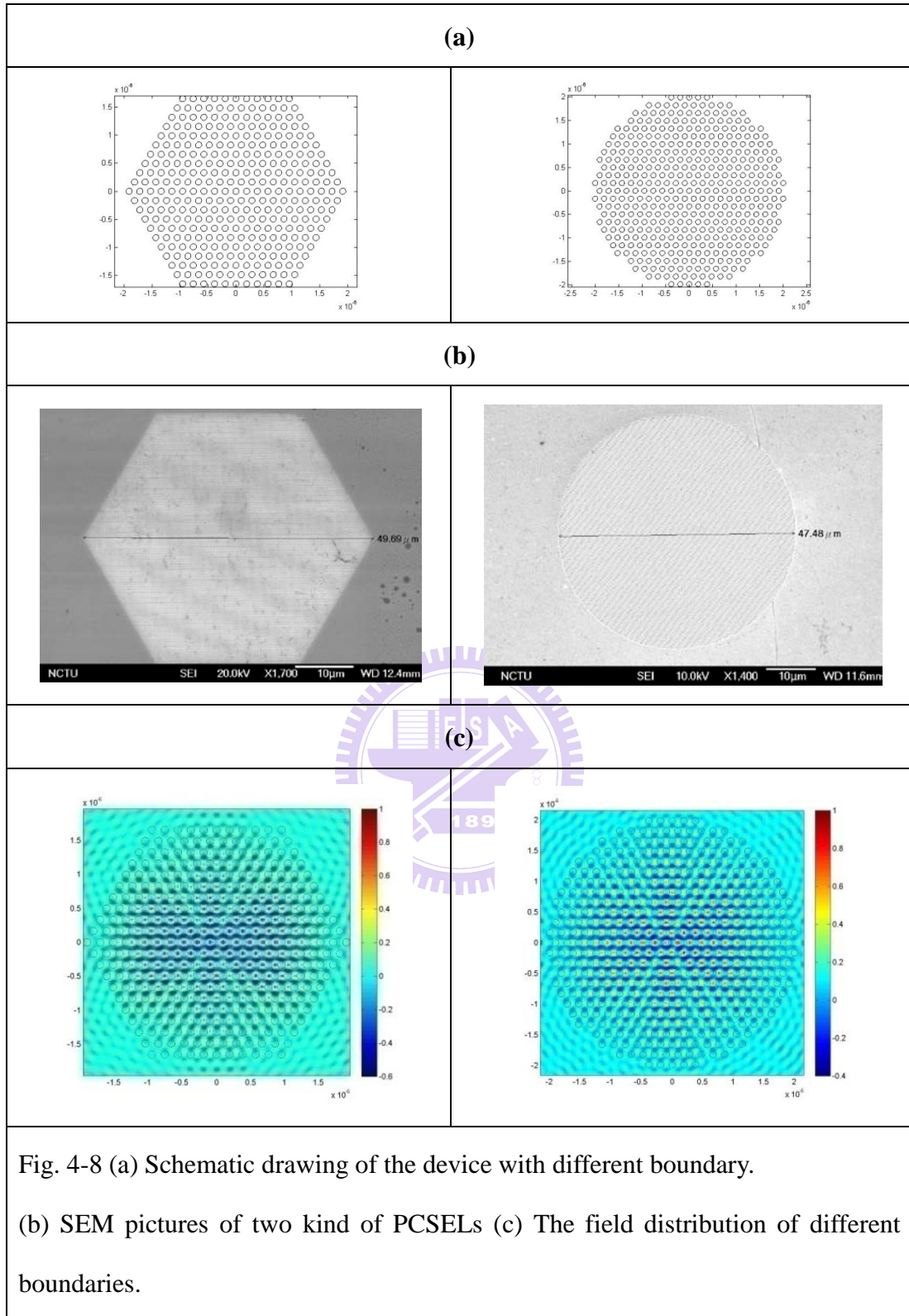
Among all the resonant modes, mode (a), mode (e) and (f) have the lowest threshold gain for  $25\% < f < 45\%$ , while mode (b) and (c) has the lowest for  $f < 20\%$  and  $35\% < f < 45\%$ . This result shows that the air-filling factor controls the mode selection scheme.

#### 4.4 The effect of Boundary for PCSEL

In this section, we will discuss the effect of boundary for PCSEL. At first, in order to investigate the lowest threshold gain value, as were already optimized the shell number and filling factor for PCSEL. However, the threshold gain was also determined by the boundary condition at the end of the cavity of the PCSELS. Here, we designed two different boundaries condition (as hexagonal, and circle boundary) to observe the difference between threshold gain and wavelength. Fig.4-8(a) shows the drawing of the device with different boundary. The hexagonal boundary is normally used in conventional photonic crystal lasers. Fig. 4-8(b) shows the SEM images with two different boundary PCSELS. The PCSELS are fabricated on the same sample by the standard process flowchart as chapter 3. The  $r/a$  ratio (where  $r$  is the radius of hole,  $a$  is the lattice constant of PC) of PCs We optical pumped the PCSELS at room temperature and the lasing intensity is shown in Figure 4-9. The clear evidence of threshold condition occurred at the pumping energy ( $E_{th}$ ) of 200 nJ and 230 nJ corresponding to an energy density of 2.8 mJ/cm<sup>2</sup> and 3.2mJ/cm<sup>2</sup> with two boundaries. In simulation results, we obtain threshold gain value and normalize frequency with different boundary condition of PCSELS by Multiple Scattering method. Based on experiment results, the lasing wavelength is 404nm, the normalized frequency  $a/\lambda$  of PCSELS is equal 0.48. Therefore, the resonant mode of simulations is the quadrupole mode of  $\Gamma_2$  oscillation based on experiment results.

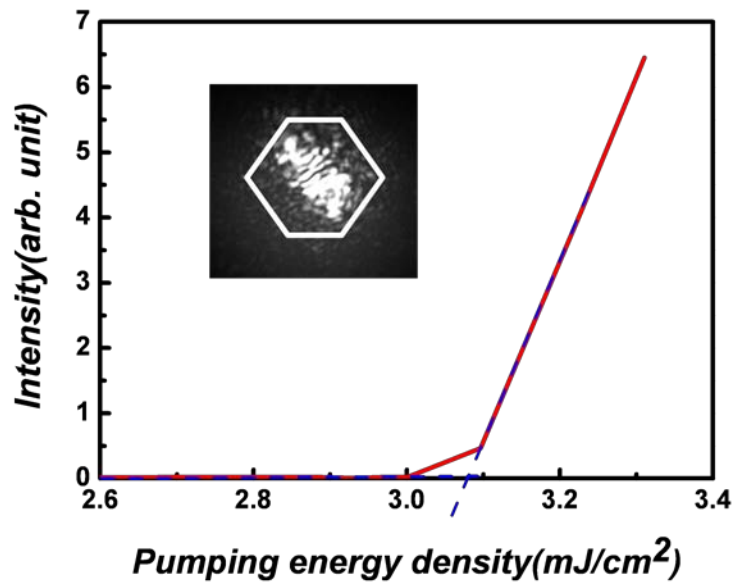
The threshold amplitude gain of hexagonal and circle boundary equals 0.003798 and 0.027837, respectively. According to the simulation and experiment results, it is reasonable and acceptable that the threshold gain of circle boundary is lower than hexagonal boundary.







(a)



(b)

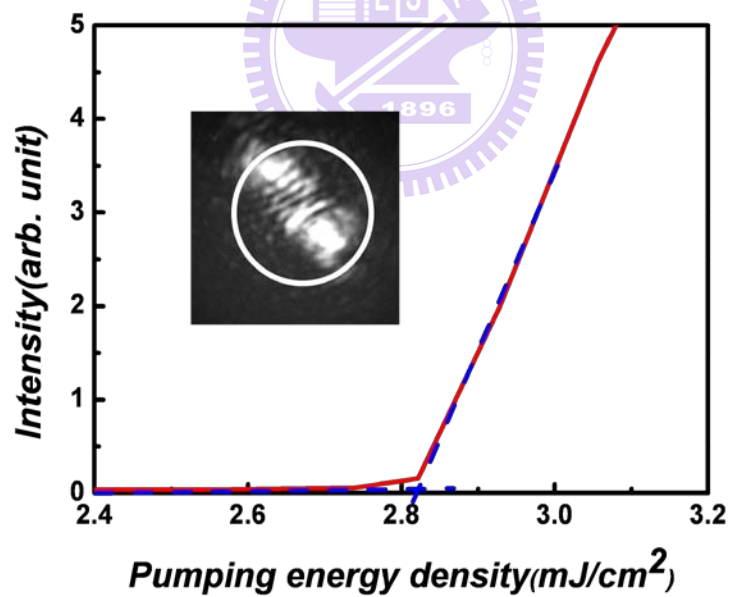


Fig. 4-9 Measured output intensity versus input excitation energy density from the GaN-based PCSELs with bottom AlN/GaN distributed Bragg reflectors at room temperature.(a)The threshold energy density of hexagonal boundary is about 3.2mJ/cm<sup>2</sup>.(b) The threshold energy density of circle boundary is about 2.85 mJ/cm<sup>2</sup>.

## Reference

- [1] H.Y. Ryu and M. Notomi PHYSICAL REVIEW B 68, 045209 (2003)
- [2] M. Yokoyama, S. Noda Optic Express, Vol. 13, No. 8, 18 April (2005)
- [3] K. Sakai, E. Miyai, and S. Noda, Optics Express Vol. 15, No. 7 April (2007)
- [4] K. Sakai, J. Yue and S. Noda, Optic Express Vol. 16, No. 9 April (2008)



# Chapter 5

## Conclusion

The simulation method of threshold gain for GaN-based photonic crystal surface emitting laser is established and measured in this thesis. We demonstrate the threshold gain, normalized frequency, and resonant mode patterns by multiple scattering method successfully. K-space simulation of investigated PCs lasing mode patterns can correspond to all band-edge frequencies ( $M1$ ,  $K1$ ,  $\Gamma2$ ,  $M2$ ,  $K2$ ,  $M3$ ), which indicates the lasing action consistent with Bragg diffraction theory. Then, the effect of shell number for PCSELS is investigated. It is obvious that the threshold gain would decrease and the normalized frequency would close to band-edge as increasing of  $N$  number. In addition, the effect of photonic crystal filling factor on the threshold gain and normalized frequency reveal that the PCSELS has the lowest threshold gain at different for different modes. The hexepole mode and quadrupole mode would have the lowest threshold gain in the filling factor is equal 0.3. However, the monopole and dipole mode would have the lowest threshold gain as smaller filling factor. Finally, we investigate the boundary condition effect to PCSELS. The circle boundary has the lower threshold gain than hexagonal boundary.

In summary, it is successful to build up a 2D simulation method for our 3D structure. However, we have to further improve the simulation techniques of GaN PCSEL to achieve the consistent with simulation results and real PCSELS by 3D simulation method. Therefore, the difference between 3D FDTD and 2D simulation method would be researched in the future.

# Appendix

r/A	filling factor	Effective index	onfinemet	$\Delta \varepsilon$	$\varepsilon a$	$\varepsilon b$	na	nb
0.166	0.1	2.482	0.8652	4.42185	2.18065871	6.60251	1.47671	2.56953
0.203	0.15	2.482	0.8652	4.42185	2.40175123	6.8236	1.54976	2.6122
0.235	0.2	2.482	0.8652	4.42185	2.62284375	7.04469	1.61952	2.65418
0.263	0.25	2.482	0.8652	4.42185	2.84393626	7.26579	1.6864	2.69551
0.288	0.3	2.482	0.8652	4.42185	3.06502878	7.48688	1.75072	2.73622
0.311	0.35	2.482	0.8652	4.42185	3.28612129	7.70797	1.81277	2.77632
0.332	0.4	2.482	0.8652	4.42185	3.50721381	7.92906	1.87276	2.81586
0.352	0.45	2.482	0.8652	4.42185	3.72830633	8.15016	1.93088	2.85485
0.371	0.5	2.482	0.8652	4.42185	3.94939884	8.37125	1.98731	2.89331
0.389	0.55	2.482	0.8652	4.42185	4.17049136	8.59234	2.04218	2.93127
0.407	0.6	2.482	0.8652	4.42185	4.39158387	8.81343	2.09561	2.96874



## Code (in Matlab System)\

Threshold gain of photonic crystal with triangle lattice

```
tic
clear
clc

%===== Parameter =====
A = 200*10^(-9);           % lattice constant
r = 0.3*A;                 % radius
c = 3*10^8;                % light velocity in free space
epi_a0 = 6.25;             % background index
epi_b0 = 1;                % rod index
mode = [1,0];              % [1,0] TE Mode , [0,1] TM Mode
S = [1,0];                 % Structure [1,0] = air hole [0,1] = rod
Shell_num = 6;             % Shellnumber of PC
Grid_N = [50,50];          % [gain grid number,frequency grid number]
W_range = [0.4,0.5];       % frequency range
Ka_range = [0.01,0.07];    % gain region
Point_Source = [5,0];      % the location of point source
L = 3;                     % expansion number of bessel function and hankel function
%=====
CenterX = Point_Source(1)*A;
CenterY = Point_Source(2)*A;
n = -L:L;                  % bessel expansion number
l = -L:L;                  % hankel expansion number
Ka_2 = (2*pi)/A*linspace(Ka_range(1),Ka_range(2),Grid_N(1));
w = (2*pi*c)/A*linspace(W_range(1),W_range(2),Grid_N(2));
%===== pattern of PC =====
% ===== Hexgonal boundary =====
Shell_num = N(3);
cp_x = CenterX;
cp_y = CenterY;

for j = 1:Shell_num
for i = 1:6
for k = 0:(j-1)
cp_x_1 = CenterX + j*A*cos(pi/3*(i-1))+k*A*cos(2*pi/3+pi/3*(i-1));
cp_y_1 = CenterY + j*A*sin(pi/3*(i-1))+k*A*sin(2*pi/3+pi/3*(i-1));
```

```

cp_x = [cp_x cp_x_1];
cp_y = [cp_y cp_y_1];
end
end
end
[col,Num_c]=size(cp_x);
cp_dx = [];
for i = 1:Num_c
    cp_dx_2 = cp_x(:,i)-cp_x;
    cp_dx = [cp_dx;cp_dx_2];
end
cp_dy = [];
for i = 1:Num_c
    cp_dy_2 = cp_y(:,i)-cp_y;
    cp_dy = [cp_dy;cp_dy_2];
end
cp_r_ij = sqrt((cp_dx).^2+(cp_dy).^2);
%===== Phi_j =====
sign_dy = sign(cp_dy);
sign_dy(find(cp_dy == 0))=1;
cp_thi_ij= sign_dy.*acos(cp_dx./cp_r_ij);
cp_thi_ij(isnan(cp_thi_ij))=0;
%===== (1-n) =====
[N_n_1,L_l_1] = meshgrid(n,1);
cp_l_n = L_l_1'-N_n_1';
%=====
cp_thi_ij = kron(cp_thi_ij,ones(2*L+1,2*L+1));
cp_r_ij = kron(cp_r_ij,ones(2*L+1,2*L+1));
cp_l_n = repmat(cp_l_n,[Num_c,Num_c]);
cp_G2 = exp(1i.*cp_l_n.*cp_thi_ij);
for mmm = 1:Grid_N(2)
    K0 = w(mmm)/c;
    for kk = 1:Grid_N(1)
        epi_a = epi_a0 - S(1)*2i*c*sqrt(epi_a0)*Ka_2(kk)/w(mmm);
        epi_b = epi_b0 - S(2)*2i*c*sqrt(epi_b0)*Ka_2(kk)/w(mmm);
        K = K0*sqrt(epi_a);
        Ka = K0*sqrt(epi_b);
        J_n = besselj(n,K*r);
    end
end

```

```

J_an = besselj(n,Ka*r);
J_n1 = besselj(n+1,K*r);
J_an1 = besselj(n+1,Ka*r);

H_n = besselh(n,1,K*r);
H_an = besselh(n,1,Ka*r);
H_n1 = besselh(n+1,1,K*r);
H_an1 = besselh(n+1,1,Ka*r);

dJ_n = n/(K*r).*J_n-J_n1;
dJ_an = n/(Ka*r).*J_an-J_an1;
dH_n = n/(K*r).*H_n-H_n1;
dH_an = n/(Ka*r).*H_an-H_an1;

g = sum(mode.*[1,epi_b/epi_a]);
h = K/Ka ;
Gama_1 = (H_n.*dJ_an - g*h*dH_n.*J_an);
Gama_2 = (g*h*dJ_n.*J_an - J_n.*dJ_an);
AAA = Gama_2./Gama_1;
S_in = repmat(AAA,[Num_c*(2*L+1),Num_c]);
cp_Gama = eye(Num_c*(2*L+1));
cp_G1 = besselh(cp_l_n,cp_r_ij*K);
cp_G = cp_G1.*cp_G2.*S_in;
cp_G(isnan(cp_G)) = 0;
cp_M = cp_Gama-cp_G;
cp_M(isinf(cp_M))=0;
cp_det_1(mm,kk) = det(cp_M);
end
end
cp_det = 1./abs(cp_det_1);
[cp_g,cp_w] = meshgrid(Ka_2*A/(2*pi),w*A/(2*pi*c));
Plot_result = surf(cp_g,cp_w,cp_det);
ylabel('wa/2fk');
xlabel('g');
zlabel('Det value');
shading interp
cd('C:\Documents and Settings\250\@à-±\MATLAB\threshold')
saveas(Plot_result,strcat('shell_5_gama', '.fig'));
Time=toc

```